crystals

MDPI

Article

Hydrothermal Synthesis, Crystal Structure, and Spectroscopic Properties of Pure and Eu^{3+}-Doped $NaY[SO_4]_2 \cdot H_2O$ and Its Anhydrate $NaY[SO_4]_2$

Constantin Buyer [1], David Enseling [2], Thomas Jüstel [2] and Thomas Schleid [1,*]

[1] Institute for Inorganic Chemistry, University of Stuttgart, D-70569 Stuttgart, Germany; buyer@iac.uni-stuttgart.de
[2] Department of Chemical Engineering, FH Münster University of Applied Sciences, D-48565 Steinfurt, Germany; david.enseling@fh-muenster.de (D.E.); tj@fh-muenster.de (T.J.)
* Correspondence: schleid@iac.uni-stuttgart.de; Tel.: +49-711/685-64240

Abstract: The water-soluble colorless compound $NaY[SO_4]_2 \cdot H_2O$ was synthesized with wet methods in a Teflon autoclave by adding a mixture of $Na_2[SO_4]$ and $Y_2[SO_4]_3 \cdot 8\,H_2O$ to a small amount of water and heating it up to 190 °C. By slow cooling, single crystals could be obtained and the trigonal crystal structure of $NaY[SO_4]_2 \cdot H_2O$ was refined based on X-ray diffraction data in space group $P3_221$ (a = 682.24(5) pm, c = 1270.65(9) pm, Z = 3). After its thermal decomposition starting at 180 °C, the anhydrate $NaY[SO_4]_2$ can be obtained with a monoclinic crystal structure refined from powder X-ray diffraction data in space group $P2_1/m$ (a = 467.697(5) pm, b = 686.380(6) pm, c = 956.597(9) pm, β = 96.8079(5), Z = 2). Both compounds display unique Y^{3+}-cation sites with eightfold oxygen coordination (d(Y–O_s = 220–277 pm)) from tetrahedral $[SO_4]^{2-}$ anions (d(S–O = 141–151 pm)) and a ninth oxygen ligand from an H_2O molecule (d(Y–O_w = 238 pm) in the hydrate case. In both compounds, the Na^+ cations are atoms (d(Na–O_s = 224–290 pm) from six independent $[SO_4]^{2-}$ tetrahedra each. Thermogravimetry and temperature-dependent PXRD experiments were performed as well as IR and Raman spectroscopic studies. Eu^{3+}-doped samples were investigated for their photoluminescence properties in both cases. The quantum yield of the red luminescence for the anhydrate $NaY[SO_4]_2$:Eu^{3+} was found to be almost 20 times higher than the one of the hydrate $NaY[SO_4]_2 \cdot H_2O$:Eu^{3+}. The anhydrate $NaY[SO_4]_2$:Eu^{3+} exhibits a decay time of about $\tau_{1/e}$ = 2.3 µm almost independent of the temperature between 100 and 500 K, while the CIE1931 color coordinates at x = 0.65 and y = 0.35 are very temperature-consistent too. Due to these findings, the anhydrate is suitable as a red emitter in lighting for emissive displays.

Keywords: sodium yttrium oxosulfate; X-ray diffraction; crystal structure; rare-earth metal compounds; luminescence; temperature- and time-dependent photoluminescence

Citation: Buyer, C.; Enseling, D.; Jüstel, T.; Schleid, T. Hydrothermal Synthesis, Crystal Structure, and Spectroscopic Properties of Pure and Eu^{3+}-Doped $NaY[SO_4]_2 \cdot H_2O$ and Its Anhydrate $NaY[SO_4]_2$. *Crystals* **2021**, *11*, 575. https://doi.org/10.3390/cryst11060575

Academic Editors: Aleksej Zarkov, Aivaras Kareiva and Loreta Tamasauskaite-Tamasiunaite

Received: 27 April 2021
Accepted: 17 May 2021
Published: 21 May 2021

1. Introduction

Eu^{3+}-doped luminescence materials based on complex oxides are very important in application [1,2] and show a red emission with typical $^5D_0 \rightarrow {}^7F_J$ transitions between 610 and 620 nm [3]. They could be prepared on "classic" solid-state routes at high temperatures, as has been done for the examples of $Y_2[MoO_4]_3$:Eu^{3+} and $Y_2[MoO_4]_2[Mo_2O_7]$:Eu^{3+} [4], $GdSb_2O_4Br$:Eu^{3+} [5], as well as $YNbO_4$:Eu^{3+} and $YTaO_4$:Eu^{3+} [6]. Another energy-saving synthesis route to get Eu^{3+}-doped luminescence materials without heating uses wet synthesis strategies. For example the Eu^{3+}-doped xenotime-type yttrium oxoarsenate $Y[AsO_4]$:Eu^{3+} [7], the oxophosphate $Y[PO_4]$:Eu^{3+} [8], and the oxocarbonate $Y_2[CO_3]_3$:$Eu^{3+} \cdot n\,H_2O$ [9] were synthesized following a wet route.

With $NaCe[SO_4]_2 \cdot H_2O$ (trigonal, $P3_121$), Lindgren reported for the first time in 1977 the crystal structure of a sodium rare-earth metal oxosulfate monohydrate yielded from

a wet synthesis by adding $Ce[OH]_3$ and $Na_2[SO_4]$ to aqueous sulfuric acid (H_2SO_4) and heating it to 230 °C for 7 days [10]. In later works of other groups, the crystal structure of the sodium rare-earth (*RE*) metal oxosulfate monohydrates $NaRE[SO_4]_2 \cdot H_2O$ for the elements *RE* = La—Nd and Sm—Dy was solved either in space group $P3_121$ (no. 152) or its enantiomorphic analog $P3_221$ (no. 154). The samples were produced by different syntheses routes [11–18] and an Indian paper from 1989 deals with these double sulfates of trivalent plutonium, as well as the rare-earth metals *RE* = La—Nd, Sm—Yb, and Y, but does not give some detailed crystallographic information except for the space group derived from powder X-ray diffraction data [19].

By changing the alkali metal sodium to the next bigger one, potassium namely, $KLa[SO_4]_2 \cdot H_2O$ emerges as the only known alkali-metal rare-earth metal oxosulfate monohydrate with the mentioned trigonal structure [20]. For the smaller rare-earth metals (*RE* = Ce—Nd, Sm—Dy), the potassium-containing oxosulfate monohydrates $KRE[SO_4]_2 \cdot H_2O$ crystallize monoclinically in space group $P2_1/c$ [20–23] in analogy to the isotypic rubidium compounds $RbRE[SO_4]_2 \cdot H_2O$ with *RE* = Ce, Gd, Ho and Yb [24–26]. For silver instead of an alkali-metal cation also $AgRE[SO_4]_2 \cdot H_2O$ representatives with the crystal structure of $NaCe[SO_4]_2 \cdot H_2O$ were found [27] and by the exchange of the rare-earth metal cation with trivalent bismuth, its oxosulfate monohydrate $NaBi[SO_4]_2 \cdot H_2O$ [28] shows the same trigonal structure as the related rare-earth metal compounds $NaRE[SO_4]_2 \cdot H_2O$.

In 2006, the photoluminescence spectrum of $NaEu[SO_4]_2 \cdot H_2O$ (excited at λ = 393 nm) [11] and in 2016 analogous spectra of $NaTb[SO_4]_2 \cdot H_2O$ (excited at λ = 320 nm) and $NaDy[SO_4]_2 \cdot H_2O$ (excited at λ = 387 nm) were measured at room temperature [12]. In 2011, Ce^{3+}- and Tb^{3+}-doped samples of $NaY[SO_4]_2 \cdot H_2O$ were the subject of a luminescence investigation [29]. Moreover, in 2015, the sodium rare-earth metal oxosulfate monohydrates $NaRE[SO_4]_2 \cdot H_2O$ with *RE* = La, Nd, and Gd could be successfully tested as heterogeneous redox catalysts for the selective oxidation of organic sulfides [13]. It is worth mentioning that $NaY[SO_4]_2 \cdot H_2O$ even occurs as a mineral with the name chinleite-(Y) [30], naturally containing all the lanthanoids with roughly the same size as yttrium. The crystallographic data from a structure refinement in space group $P3_221$ have never been deposited at a common database, however.

For the anhydrous sodium rare-earth metal oxosulfates $NaRE[SO_4]_2$, their monoclinic crystal structure was solved in space group $P2_1/m$ for *RE* = Er [31] and Tm [32] and the triclinic one in space group $P\bar{1}$ for *RE* = La [33] and Nd [31]. For trivalent gold instead of RE^{3+} cations, the monoclinic crystal structure of $NaAu[SO_4]_2$ was described in space group $P2_1/n$ [34], but Au^{3+} in square planar oxygen coordination causes marked topological differences. Not so different from the Na^+ analogs, for triclinic $AgEu[SO_4]_2$ (space group: $P\bar{1}$) with Ag^+ in eightfold oxygen coordination, its Eu^{3+} bulk luminescence was also measured very recently [35].

In the following contribution, we report on the preparation of $NaY[SO_4]_2 \cdot H_2O$ via wet synthesis, its trigonal crystal structure, and the red luminescence of Eu^{3+}-doped samples. After thermal decomposition, we obtained its monoclinic anhydrate $NaY[SO_4]_2$, which shows an even stronger red luminescence, when Eu^{3+}-doped.

2. Materials and Methods

2.1. Synthesis

Sodium yttrium oxosulfate monohydrate $NaY[SO_4]_2 \cdot H_2O$ was obtained from a wet synthesis by adding 6.6 mmol $Na_2[SO_4]$ (ChemPur, 99.9%) and 5.5 mmol $Y_2[SO_4]_3 \cdot 8\,H_2O$, which means an excess of $Na_2[SO_4]$, to about 4 ml demineralized water and heated the obtained wet powder to 190 °C in a 25 ml Teflon autoclave overnight, with a yield only limited by the solubility of the monohydrate. Thus, the yield was about $^2/_3$ of the theoretical possible quantity. It could be increased by evaporating the water, but the change of contamination with $Y_2[SO_4]_3 \cdot 8\,H_2O$ becomes higher then. By slowly cooling the solution down (5 °C per 1 h), single crystals in a size up to 0.3 mm edge length

(Figure 1) of the water-soluble colorless compound $NaY[SO_4]_2 \cdot H_2O$ could be isolated (Equation (1)) and washed with ethanol (Brüggemann, denaturized with petrol ether). The starting material $Y_2[SO_4]_3 \cdot 8\ H_2O$ was synthesized by evaporating a solution of Y_2O_3 (ChemPur, 99.9%) in 96% sulfuric acid H_2SO_4 (Scharr, pure) according to Equation (2).

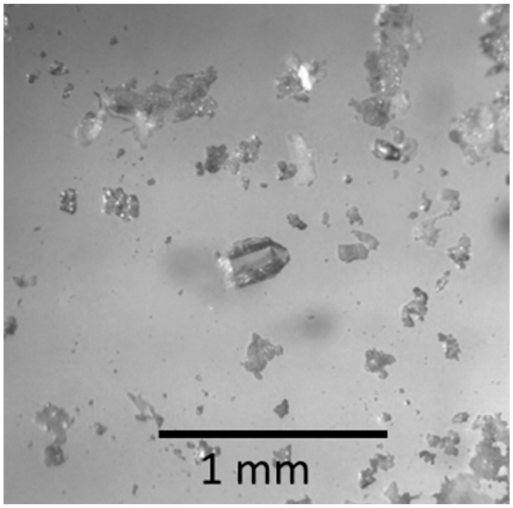

Figure 1. Colorless single crystals of $NaY[SO_4]_2 \cdot H_2O$.

The anhydrous oxosulfate $NaY[SO_4]_2$ can be obtained by heating $NaY[SO_4]_2 \cdot H_2O$ in air at a temperature of 180 °C or higher (Equation (3)). The powder, which was used for the crystal structure refinement, was drained at 550 °C. For the luminescence measurements, a Eu^{3+}-doped sample of $NaY[SO_4]_2 \cdot H_2O$ (0.5% Eu instead of Y) was produced by adding $Eu_2[SO_4]_3 \cdot 8\ H_2O$ (synthesis analogous to $Y_2[SO_4]_3 \cdot 8\ H_2O$ with Eu_2O_3 (ChemPur, 99.9%) instead of Y_2O_3) to the process, which is described in Equation (1), and $NaY[SO_4]_2$:Eu^{3+} has been prepared by draining the doped sample at 550 °C in air.

$$Na_2[SO_4] + Y_2[SO_4]_3 \cdot 8\ H_2O \rightarrow 2\ NaY[SO_4]_2 \cdot H_2O + 7\ H_2O \quad (1)$$

$$RE_2O_3 + 3\ H_2SO_4 + 5\ H_2O \rightarrow RE_2[SO_4]_3 \cdot 8\ H_2O\ (RE = \text{Y and Eu}) \quad (2)$$

$$NaY[SO_4]_2 \cdot H_2O \rightarrow NaY[SO_4]_2 + H_2O \uparrow \quad (3)$$

2.2. X-ray Experiments and Crystal-Structure Solution

For single-crystal X-ray diffraction experiments, a suitable crystal was selected under a light microscope and fixed inside of a glass capillary with an outer diameter of 0.1 mm and a length of about 15 mm. The crystal was measured with a κ-CCD four-circle X-ray diffractometer (Bruker Nonius, Karlsruhe, Germany) with Mo-Kα radiation (λ = 71.07 pm) at 293 K (room temperature). Crystal-structure solution and refinement for $NaY[SO_4]_2 \cdot H_2O$ (CSD-2016596) in the trigonal space group $P3_221$ were carried out with the program package SHELX-97 [36,37] by Sheldrick, and the program HABITUS by Bärninghausen and Herrendorf was applied [38] for a numerical absorption correction.

For X-ray powder diffraction (PXRD), part of the sample was fixed on a STADI-P diffractometer (Stoe & Cie, Darmstadt, Germany) and measured with Cu-Kα radiation (λ = 154.06 pm) in transmission setting. The monohydrate was measured from 2θ = 10–90° for checking phase purity and the anhydrate $NaY[SO_4]_2$ (CSD-2072719) was measured from 2θ = 8–110° for solving its crystal structure in the $NaEr[SO_4]_2$-type arrangement [31] with the program FULLPROF [39,40]. The measured powder X-ray diffraction pattern of $NaY[SO_4]_2 \cdot H_2O$ can be seen in Figure 2 (top) and the measured PXRD pattern together with the difference plot of the Rietveld refinement for $NaY[SO_4]_2$ is shown in Figure 2 (bottom).

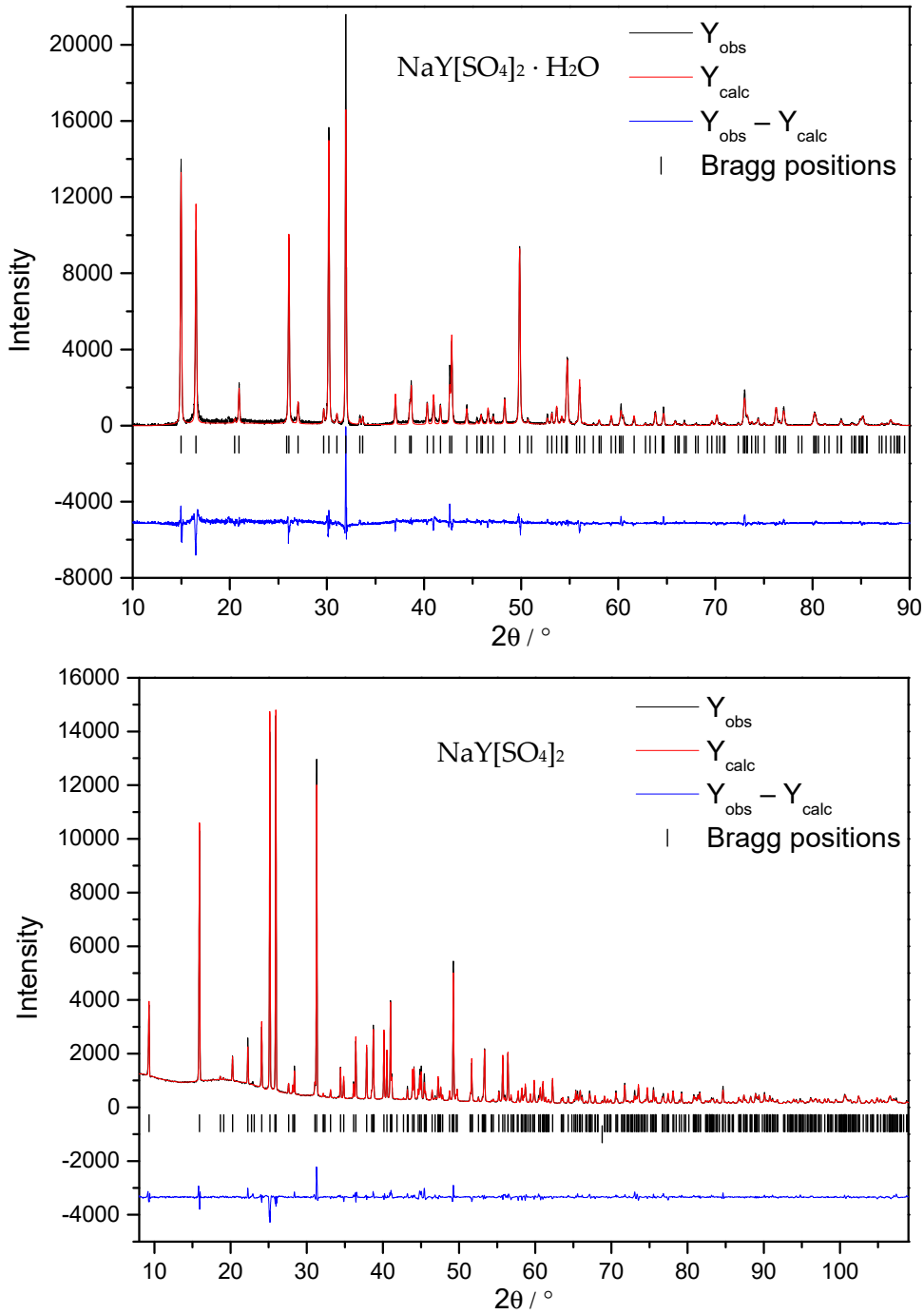

Figure 2. Rietveld refinement based on PXRD data of $NaY[SO_4]_2 \cdot H_2O$ (**top**) for checking its phase purity and $NaY[SO_4]_2$ (**bottom**) for crystal-structure determination and refinement.

Temperature-depending powder X-ray diffraction data were measured in the interval 2θ = 10–90° with a RIGAKU SmartLab diffractometer (Neu-Isenburg, Germany) using Cu-Kα radiation (λ = 154.06 pm) in reflection setting from 25 up to 900 °C.

While all the atomic displacement parameters of $NaY[SO_4]_2 \cdot H_2O$ could be refined anisotropically based on single-crystal X-ray diffraction data, the atomic displacement parameters of $NaY[SO_4]_2$ were only treated isotropically with Rietveld refinement based on PXRD data.

2.3. Thermal Analysis

Thermal analysis (thermogravimetry) was performed with about 36 mg of a $NaY[SO_4]_2 \cdot H_2O$ samples with a Netzsch device of the type STA-449C (Selb, Germany) in a corundum crucible under argon atmosphere. The sample was heated with 5 K/min from 25 to 1400 °C.

2.4. Luminescence Spectroscopy

Excitation and emission spectra were collected using a fluorescence spectrometer FLS920 (Edinburgh Instruments, Livingston, UK) equipped with a 450 W ozone-free xenon discharge lamp (Osram, München, Germany) and a cryostat "MicrostatN" from Oxford Instruments (Abingdon, UK) as the sample chamber. Additionally, a mirror optic for powder samples was applied. For detection, an R2658P single-photon-counting photomultiplier tube (Hamamatsu, Hamamatsu, Japan) was used. All photoluminescence spectra were recorded with a spectral resolution of 0.5 nm and a dwell time of 0.5 s in 0.5 nm steps.

The photoluminescence decay times were measured on an FLS920 spectrometer (Edinburgh Instruments, Livingston, UK). A Xe µ-flash lamp µF920 was used as an excitation source. For detection, an R2658P single-photon-counting photomultiplier tube (Hamamatsu Photonics, Hamamatsu, Japan) found application.

For the reflection spectra, the investigated samples were placed into an integrating sphere, and FLS920 spectrometer (Edinburgh Instruments, Livingston, UK) equipped with a 450 W Xe lamp, and a cooled (−20 °C) single-photon-counting photomultiplier (Hamamatsu R928) was used. $Ba[SO_4]$ was applied as the reflectance standard. The excitation and emission bandwidths were 10.00 and 0.06 nm, respectively. Step width was 0.5 nm and integration time 0.5 s.

Quantum yields were determined according to the method published by Kawamura et al. [41] upon excitation at 395 nm using a 7 nm excitation and 0.5 nm emission slit. The scan steps were 0.5 nm, while the respective emission intensity from 370 to 750 nm was recorded.

The CIE1931 color coordinates and luminous efficacy (*LE*) values were calculated from the temperature-dependent emission spectra of $NaY[SO_4]_2{:}Eu^{3+}$ using the Color Calculator 6.75 software from Osram (Osram, München, Germany) [42].

The *LE* value (unit: lm/W) is a parameter describing, how bright the radiation is perceived by an average human observer at a photopic illumination situation. It scales with the photopic human eye sensitivity curve *V(λ)* and can be calculated from the normalized emission spectrum *I(λ)* of the sample as follows [43]:

$$LE(\mathrm{lm/W}) = 683\ (\mathrm{lm/W}) \cdot \frac{\int_{380\mathrm{nm}}^{780\mathrm{nm}} I(\lambda)V(\lambda)d\lambda}{\int_{380\mathrm{nm}}^{780\mathrm{nm}} I(\lambda)d\lambda}$$

2.5. IR and Raman Spectra

Infrared spectra for powder samples of $NaY[SO_4]_2 \cdot H_2O$ and $NaY[SO_4]_2$ was measured from 700 to 4000 cm^{-1} with a NICOLET iS5 device from Thermo Scientific (Karlsruhe, Germany). Raman spectroscopy was performed with a DXR SmartRaman spectrometer from Thermo Scientific (Karlsruhe, Germany) with a red laser (λ = 780 nm) and a laser power of 10 mW from 200 to 1800 cm^{-1}.

3. Results and Discussion

3.1. Structure Refinement and Description of $NaY[SO_4]_2 \cdot H_2O$ and $NaY[SO_4]_2$

The most relevant crystallographic data of the wet synthesized $NaY[SO_4]_2 \cdot H_2O$ compared to its anhydrate $NaY[SO_4]_2$ are shown in Table 1. The given lattice parameters of $NaY[SO_4]_2 \cdot H_2O$ stems from single-crystal data, while its lattice parameters from PXRD experiments amount to a = 682.82(3) pm and c = 1270.77(6) pm (c/a = 1.861).

Table 1. Crystallographic data of $NaY[SO_4]_2 \cdot H_2O$ (**left**) and $NaY[SO_4]_2$ (**right**).

Compound	**$NaY[SO_4]_2 \cdot H_2O$**	**$NaY[SO_4]_2$**
Crystal system	trigonal	monoclinic
Space group	$P3_221$ (no. 154)	$P2_1/m$ (no. 11)
Lattice parameters,		
a [pm]	682.24(5)	467.697(5)
b [pm]	$= a$	686.380(6)
c [pm]	1270.65(9)	956.597(9)
β [°]	90	96.8079(5)
Number of formula units, Z	3	2
Unit-cell volume, V_{uc} [nm^3]	0.51219(4)	0.304919(5)
Molar volume, V_m [$cm^3 \cdot mol^{-1}$]	102.81	91.81
Calculated density, D_x [$g \cdot cm^{-3}$]	3.132	3.311
Diffraction method	single crystal	powder
Instrument	κ-CCD	Stadi-P (transmission)
Radiation	Mo-Kα, λ = 71.07 pm	Cu-Kα, λ = 154.06 pm
Structure resolution and refinement	SHELX-97	FULLPROF
Range in $\pm h$, $\pm k$, $\pm l$	8, 8, 16	4, 7, 10
Range of 2θ [°]	3–55	8–110
Absorption coefficient, μ [mm^{-1}]	19.25	–
Extinction coefficient, g	0.0174(15)	–
Reflections collected	8159	438
and unique	786	–
R_{int} / R_σ	0.080/0.036	–
R_1 / wR_2 for all reflections	0.031/0.070	–
Goodness of Fit (GooF)	1.074	–
Residual e^- density (max. / min.)	0.60 and −0.48	–
Flack-x parameter	−0.021(9)	–
R_p	–	4.67
R_{wp}	–	7.52
R_{exp}	–	4.33
χ^2	–	3.02
CSD number	2016596	2072719

Table 2 shows the fractional atomic coordinates with the site symmetry for all atoms and U_{eq} or U_{iso} values of $NaY[SO_4]_2 \cdot H_2O$ and $NaY[SO_4]_2$.

While $NaY[SO_4]_2 \cdot H_2O$ crystallizes in the trigonal space group $P3_221$ (no. 154) with a = 682.24(5) pm, and c = 1270.65(9) pm (c/a = 1.862) for Z = 3, $NaY[SO_4]_2$ adopts the monoclinic space group $P2_1/m$ (no. 11) with a = 467.697(5) pm, b = 686.380(6) pm, c = 956.597(10) pm, and β = 96.8079(5)° for Z = 2. The b-axes of both compounds differ by only 0.6% and the c-axis of the monohydrate is about $^4/_3$ of the one of the anhydrate. While in the hydrate monolayers of Na^+ and Y^{3+} cations take turns along [001], in the anhydrate double layers of each Na^+ and Y^{3+} alternate along [001]. Extended unit cells of $NaY[SO_4]_2 \cdot H_2O$ and $NaY[SO_4]_2$ can be seen in Figure 3.

In $NaY[SO_4]_2 \cdot H_2O$, the Y^{3+} cations are coordinated by nine oxygen atoms (eight from oxosulfate anions (d(Y–O) = 237–248 pm) and one from a water molecule (d(Y–O5w) = 238 pm). Only eight oxygen atoms covalently bonded to sulfur in $[SO_4]^{2-}$, and units occur as Y^{3+} coordination sphere (d(Y–O) = 220–277 pm) in $NaY[SO_4]_2$.

Table 2. Fractional atomic coordinates, site symmetry and *U* values * of $NaY[SO_4]_2 \cdot H_2O$ (top) and $NaY[SO_4]_2$ (bottom).

Atom	*Wyckoff* Site	Symmetry	*x/a*	*y/b*	*z/c*	*U*/pm^2
Na	3*b*	.2.	0.5299(3)	0	$^1/_6$	211(5)
Y	3*a*	.2.	0	0.56341(8)	$^1/_3$	145(2)
S	6*c*	1	0.9864(2)	0.5437(2)	0.09243(6)	134(2)
O1	6*c*	1	0.1273(5)	0.5055(5)	0.0180(2)	217(7)
O2	6*c*	1	0.8273(5)	0.5829(5)	0.0316(2)	210(7)
O3	6*c*	1	0.8677(5)	0.3517(5)	0.1655(2)	192(7)
O4	6*c*	1	0.1249(5)	0.7408(5)	0.1610(2)	196(7)
O5w	3*a*	.2.	0	0.9123(8)	$^1/_3$	369(14)
H	6*c*	1	0.063(11)	0.957(11)	0.042(4)	554(36)
Na	2*e*	*m*	0.6289(11)	$^1/_4$	0.3506(4)	195(12)
Y	2*e*	*m*	0.6536(3)	$^1/_4$	0.82110(12)	167(3)
S1	2*e*	*m*	0.1619(7)	$^1/_4$	0.5875(3)	163(9)
S2	2*e*	*m*	0.1407(6)	$^1/_4$	0.0715(3)	183(9)
O1	2*e*	*m*	0.8254(13)	$^1/_4$	0.0738(6)	114(18)
O2	2*e*	*m*	0.2317(13)	$^1/_4$	0.9259(6)	105(17)
O3	4*f*	1	0.3075(10)	0.0730(6)	0.6574(4)	177(14)
O4	4*f*	1	0.2628(10)	0.0699(6)	0.1470(4)	176(13)
O5	2*e*	*m*	0.8757(14)	$^1/_4$	0.6311(6)	119(18)
O6	2*e*	*m*	0.1881(13)	$^1/_4$	0.4401(6)	106(18)

* *U* values for $NaY[SO_4]_2 \cdot H_2O$: $U_{eq} = {}^1/_3\,[U_{33} + {}^4/_3\,(U_{11} + U_{22} - U_{12})]$ [44], but for all atoms of $NaY[SO_4]_2$ and H of $NaY[SO_4]_2 \cdot H_2O$: U_{iso}.

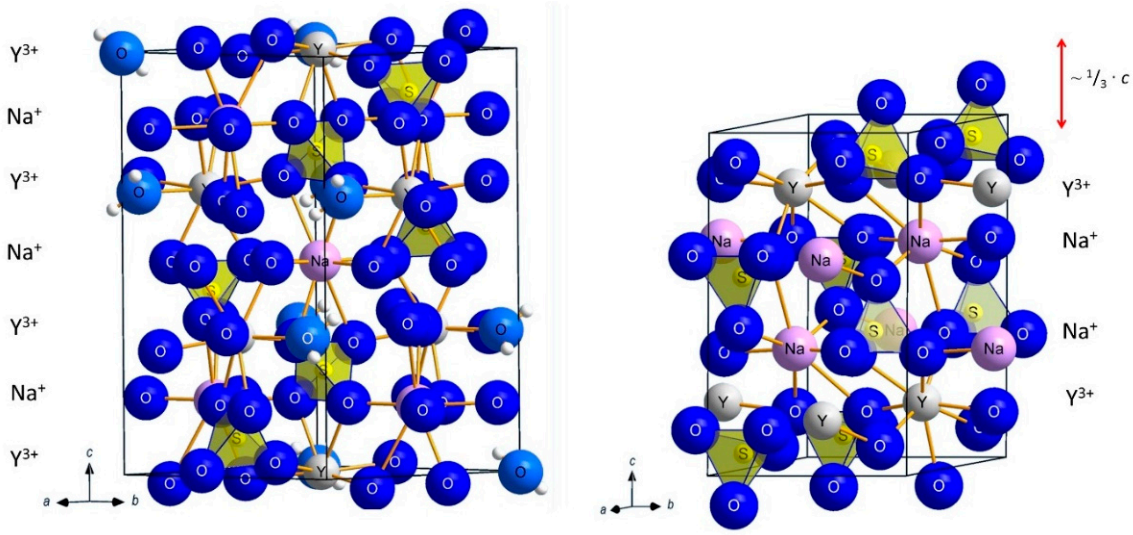

Figure 3. Extended unit cells of $NaY[SO_4]_2 \cdot H_2O$ (**left**) and $NaY[SO_4]_2$ (**right**). While in $NaY[SO_4]_2 \cdot H_2O$ monolayers of Na^+ and Y^{3+} alternate along [001], in $NaY[SO_4]_2$ double layers of each Na^+ and Y^{3+} do so.

Y^{3+} in $NaY[SO_4]_2 \cdot H_2O$ resides on the Wyckoff site 3*a* with C_2 symmetry (Figure 4, left), whereas Y^{3+} in $NaY[SO_4]_2$ occupies the 2*e* position on a mirror plane (Figure 4, right).

In $Y_2[SO_4]_3 \cdot 8\,H_2O$ [45], the unique Y^{3+} cations are also surrounded by eight oxygen atoms (four from water molecules and four more from oxosulfate anions) with distances between 230 and 247 pm, while in the anhydrous oxosulfate $Y_2[SO_4]_3$, Y^{3+} is surrounded octahedrally by only six oxygen atoms from oxosulfate groups with distances between 220 and 224 pm [46]. While Y^{3+} is coordinated by just one oxygen atom per $[SO_4]^{2-}$ anion in both $Y_2[SO_4]_3 \cdot 8\,H_2O$ [45] and $Y_2[SO_4]_3$ [46], the same is observed in $NaY[SO_4]_2 \cdot H_2O$ and $NaY[SO_4]_2$, but now with two oxygen atoms of the same oxosulfate unit. In $Y_2[SO_4]_3$ [46], $NaY[SO_4]_2 \cdot H_2O$ and $NaY[SO_4]_2$ six $[SO_4]^{2-}$ anions coordinate the Y^{3+}

cations, while in $Y_2[SO_4]_3 \cdot 8\ H_2O$ [45] there are only four of them. Compounds of the type $ARE[SO_4]_2 \cdot H_2O$ with A = Na crystallize trigonally in space group $P3_221$ (or $P3_121$) [10–18], but monoclinically in space group $P2_1/c$ with A = K for RE = Ce—Nd, Sm—Dy [20–23]. The water molecule in $NaY[SO_4]_2 \cdot H_2O$ is only coordinated to yttrium, whereas in the $KRE[SO_4]_2 \cdot H_2O$ examples [20–23], it further coordinates the alkali-metal cation. The crystal structure of the anhydrous potassium rare-earth metal oxosulfates are described triclinically in space group $P\bar{1}$ for RE = Pr [47] and Nd [48], but monoclinically in space group $P2_1/c$ for RE = Nd [49] and Er [50]. In the triclinic structure, the coordination number of RE^{3+} is eight, while in the monoclinic one, it surprisingly increases to nine. Two oxosulfate anions coordinate with two oxygen atoms each in the monoclinic $KRE[SO_4]_2$ representatives, while in the triclinic cases only one $[SO_4]^{2-}$ group has two contacts to the rare-earth metal cations. The coordination environments of those in the two title compounds are compared to the other alkali-metal rare-earth metal oxosulfates in Figure 5.

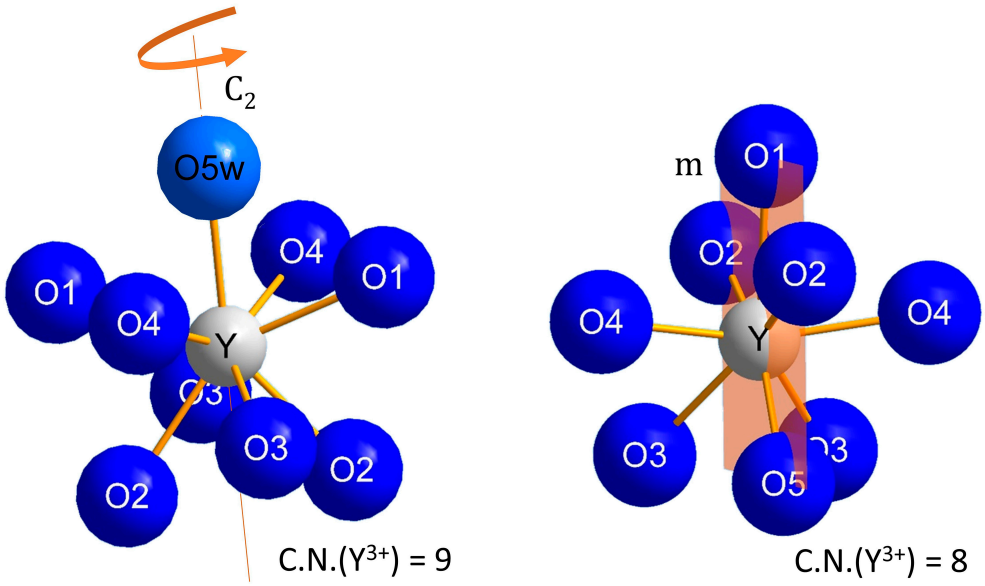

Figure 4. Y^{3+} is coordinated by nine oxygen atoms in $NaY[SO_4]_2 \cdot H_2O$ with C_2 symmetry (**left**) and by eight oxygen atoms in $NaY[SO_4]_2$ residing in a mirror plane (**right**).

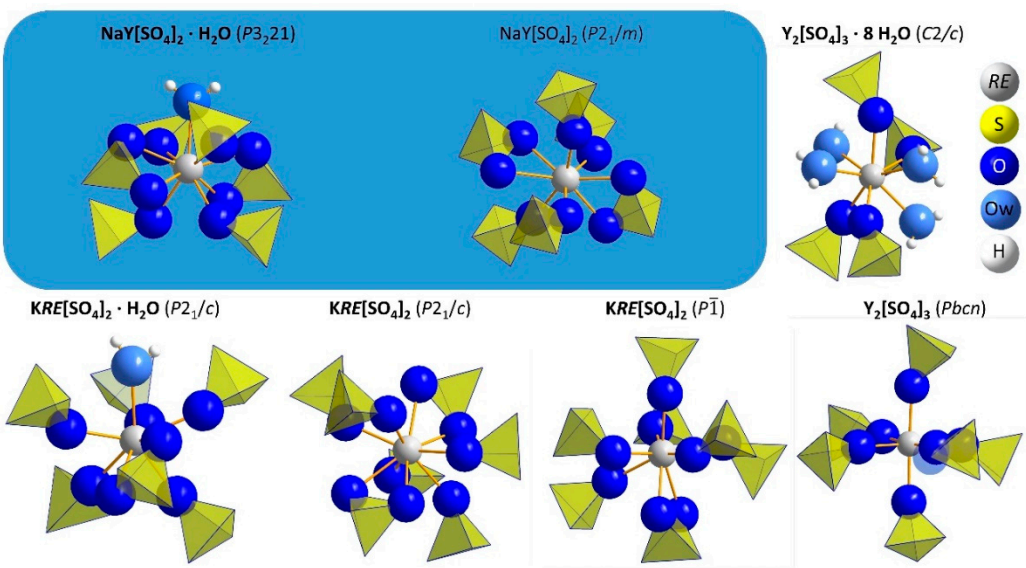

Figure 5. Coordination spheres of the RE^{3+} cations in different rare-earth metal oxosulfates. The blue box contains the title compounds $NaY[SO_4]_2 \cdot H_2O$ and $NaY[SO_4]_2$.

The sodium cations in both title compounds are surrounded by eight oxygen atoms from six different oxosulfate units as a bicapped octahedron. While Na^+ in $NaY[SO_4]_2 \cdot H_2O$ is only connected with $[SO_4]^{2-}$ anions and no water molecules, in the related potassium compound the K^+ cation has contact with six of them and one water molecule [20–23]. The anhydrous potassium rare-earth metal oxosulfates show a coordination sphere around the alkali-metal cation erected by ten oxygen atoms from six oxosulfate anions in case of the triclinic examples [47,48] and seven terminal $[SO_4]^{2-}$ units in the monoclinic cases [49,50]. In the orthorhombic salt $Na_2[SO_4]$, the sodium cations show six oxygen atoms from five oxosulfate groups as next neighbors [51], while in its decahydrate $Na_2[SO_4] \cdot 10\ H_2O$, Na^+ is only surrounded by six water molecules octahedrally [52] (Figure 6).

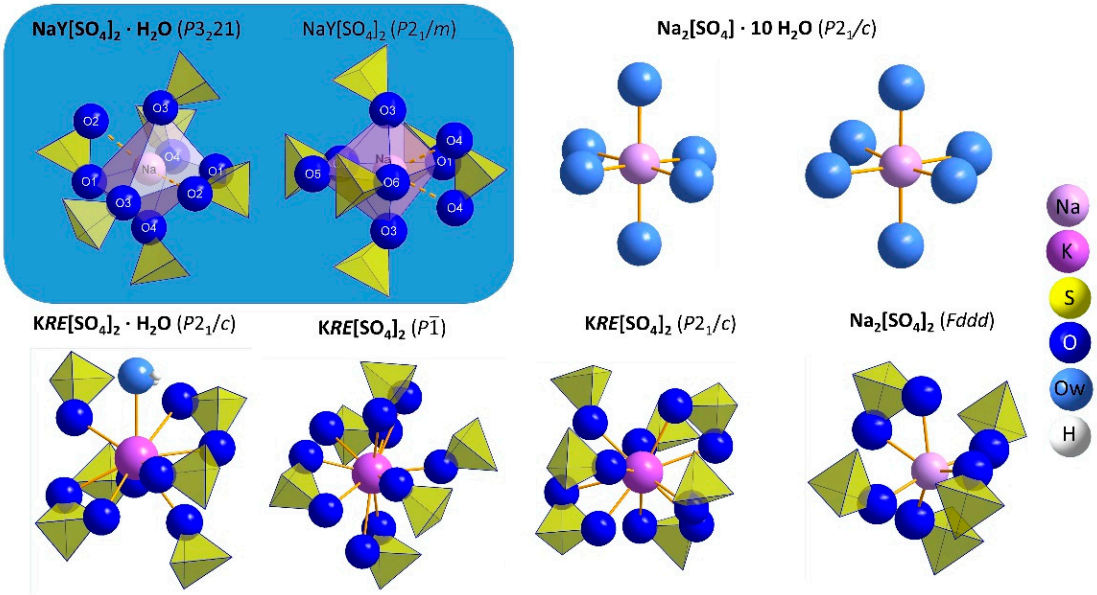

Figure 6. Coordination spheres of the alkali-metal cations (A = Na and K) in different oxosulfates. The blue box contains the title compounds $NaY[SO_4]_2 \cdot H_2O$ and $NaY[SO_4]_2$.

While $NaY[SO_4]_2 \cdot H_2O$ exhibits only one singular crystallographic $[SO_4]^{2-}$ anion, its anhydrate has two different ones of them (Figure 7). All oxygen atoms in $NaY[SO_4]_2 \cdot H_2O$ are surrounded approximately in a plane triangular fashion by Y^{3+}, $Na^{+,}$ and S^{6+}, while in $NaY[SO_4]_2$ O2 and O6 differ from this scheme since O2 is coordinated by one S^{6+} and two Y^{3+} and O6 by one S^{6+} and two Na^+ cations. Even O5w has one Y^{3+} and two H^+ cations, three neighbors. The triangular environments of the oxygen atoms in $NaY[SO_4]_2 \cdot H_2O$ and $NaY[SO_4]_2$ can be seen in Figure 8. Selected interatomic distances (d/pm) are summarized in Table 3.

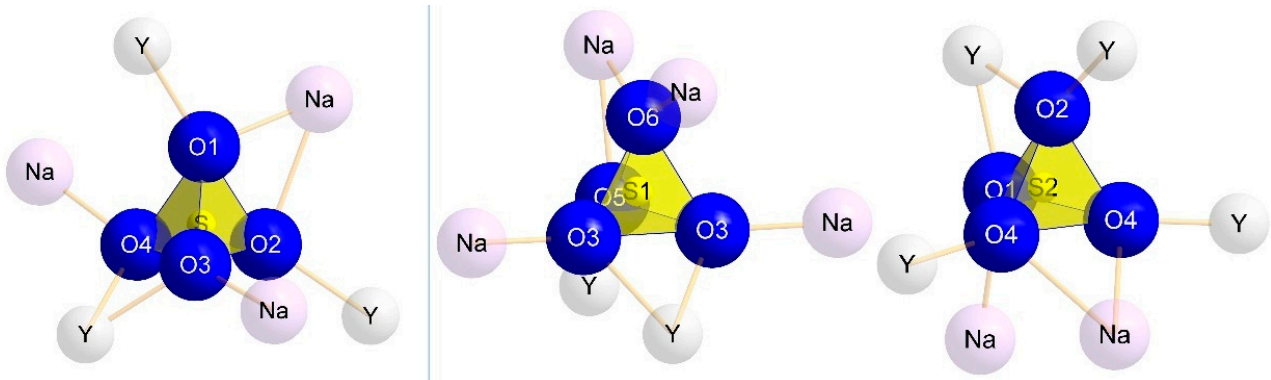

Figure 7. Coordination spheres of the tetrahedral oxosulfate anions $[SO_4]^{2-}$ in $NaY[SO_4]_2 \cdot H_2O$ (**left**) and $NaY[SO_4]_2$ (**right**).

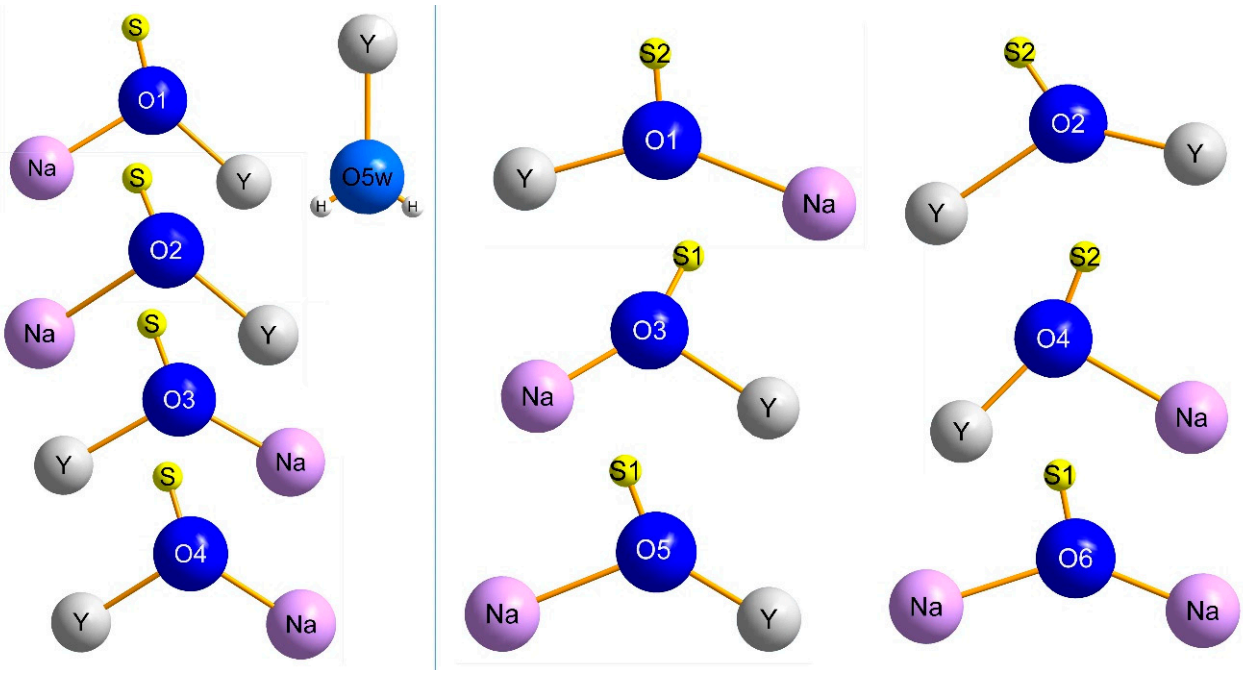

Figure 8. Coordination spheres of the oxygen atoms in $NaY[SO_4]_2 \cdot H_2O$ (**left**) and $NaY[SO_4]_2$ (**right**).

Table 3. Selected interatomic distances (d/pm) in the crystal structures of $NaY[SO_4]_2 \cdot H_2O$ (**left**) and $NaY[SO_4]_2$ (**right**).

$NaY[SO_4]_2 \cdot H_2O$			**$NaY[SO_4]_2$**		
d(Y–O2)	(1×)	236.7(3)	d(Y–O5)	(1×)	219.8(7)
d(Y–O2)	(1×)	239.7(4)	d(Y–O4)	(2×)	224.5(4)
d(Y–O5$_W$)	(1×)	238.0(3)	d(Y–O2)	(1×)	231.7(6)
d(Y–O1)	(2×)	239.1(3)	d(Y–O3)	(2×)	243.9(4)
d(Y–O4)	(2×)	224.0(3)	d(Y–O1)	(1×)	245.5(6)
d(Y–O3)	(2×)	247.9(3)	d(Y–O2)	(1×)	277.0(6)
$\bar{d}$(Y–O)	(C.N. = 9)	241.5	$\bar{d}$(Y–O)	(C.N. = 8)	238.8
d(Na–O3)	(2×)	235.4(4)	d(Na–O3)	(2×)	223.9(4)
d(Na–O4)	(2×)	242.5(4)	d(Na–O6)	(1×)	232.4(8)
d(Na–O1)	(2×)	253.6(3)	d(Na–O6)	(1×)	265.4(8)
d(Na–O2)	(2×)	287.9(3)	d(Na–O4)	(2×)	273.2(5)
$\bar{d}$(Na–O)	(C.N. = 8)	254.9	d(Na–O5)	(1×)	279.3(7)
			d(Na–O1)	(1×)	290.4(7)
			$\bar{d}$(Na–O)	(C.N. = 8)	257.7
d(S–O1)	(1×)	146.2(3)			
d(S–O2)	(1×)	146.2(4)	d(S1–O6)	(1×)	141.0(7)
d(S–O3)	(1×)	147.4(3)	d(S1–O5)	(1×)	144.9(8)
d(S–O4)	(1×)	148.0(3)	d(S1–O3)	(2×)	151.0(4)
$\bar{d}$(S–O)	(C.N. = 4)	147.2	$\bar{d}$(S1–O)	(C.N. = 4)	147.4
			d(S2–O1)	(1×)	147.7(7)
			d(S2–O2)	(1×)	150.4(7)
			d(S2–O4)	(2×)	150.9(4)
			$\bar{d}$(S2–O)	(C.N. = 4)	150.0

For confirmation of the Na^+ and Y^{3+} sites in $NaY[SO_4]_2 \cdot H_2O$ and $NaY[SO_4]_2$, bond-valence calculations were carried out with the parameters used by Brese and O'Keeffe [53]. With calculated charges of 3.06 in $NaY[SO_4]_2 \cdot H_2O$ and 3.19 in $NaY[SO_4]_2$ for the Y^{3+} sites next to 1.20 in $NaY[SO_4]_2 \cdot H_2O$ and 1.23 in $NaY[SO_4]_2$ for the Na^+ sites, their positions can just be confirmed. More details of these calculations can be seen in Table 4. The bond-

valence equation for the calculation of the charge given by Brese and O'Keeffe [53] is $v_{ij} = \exp[(R_{ij} - d_{ij})/b]$ with the valence v_{ij}, the universal constant b = 0.37 Å, the bond-valence parameter $R_{ij,}$ and the Ångström distance of the considered atoms d_{ij} between the atoms **i** and **j**. The sum $\sum(v_{ij})$ represents the charge of the regarded ion.

Table 4. Results of the bond-valence calculations for $NaY[SO_4]_2 \cdot H_2O$ and $NaY[SO_4]_2$.

$NaY[SO_4]_2 \cdot H_2O$										
for Y	O2	O2′	O5	O1	O1′	O4	O4′	O3	O3′	
d(Y–O) [pm]	236.68	236.70	238.03	239.12	239.13	243.98	244.06	247.86	247.93	$\sum(v_{ij})$
v_{ij}	0.385	0.385	0.372	0.361	0.361	0.316	0.316	0.285	0.284	**3.065**
for Na	O3	O3′	O4	O4′	O1	O1′	O2	O2′		
d(Na–O) [pm]	235.35	235.35	242.50	242.50	253.58	253.66	287.92	287.99		$\sum(v_{ij})$
v_{ij}	0.224	0.224	0.185	0.185	0.137	0.137	0.054	0.054		**1.199**
for S	O1	O2	O3	O4			**for H**		O5w	
d(S–O) [pm]	101.46	101.46	101.47	101.48	$\sum(v_{ij})$		d(H–O) [pm]		97.86	
v_{ij}	1.550	1.549	1.500	1.477	**6.076**			v_{ij}	**0.926**	
$NaY[SO_4]_2$										
for Y	O5	O4	O4	O2	O3	O3	O1	O2		
d(Y–O) [pm]	219.77	224.48	224.48	231.68	243.87	243.87	245.53	277.00		$\sum(v_{ij})$
v_{ij}	0.609	0.536	0.536	0.441	0.317	0.317	0.303	0.130		**3.189**
for Na	O3	O3′	O6	O6′	O4	O4′	O5	O1		
d(Na–O) [pm]	223.94	223.94	232.42	265.37	272.18	273.18	279.25	290.39		$\sum(v_{ij})$
v_{ij}	0.305	0.305	0.242	0.100	0.083	0.081	0.068	0.051		**1.234**
for S1	O6	O5	O3 (2×)		**for S2**		O1	O2	O4 (2×)	
d(S1–O) [pm]	142.97	144.85	150.96	$\sum(v_{ij})$	d(S2–O) [pm]		147.74	150.39	150.93	$\sum(v_{ij})$
v_{ij}	1.691	1.607	1.362	**6.022**		v_{ij}	1.486	1.383	1.363	**5.597**
R_{ij} constant from [53] for			Y	Na	S	H				
	distance to O		2.014	1.80	1.624	0.95	Å			

The motifs of mutual adjunction for the atoms in both title compounds $NaY[SO_4]_2 \cdot H_2O$ and $NaY[SO_4]_2$ can be seen in Table 5.

Table 5. Motifs of mutual adjunction for $NaY[SO_4]_2 \cdot H_2O$ (top) and $NaY[SO_4]_2$ (bottom).

$NaY[SO_4]_2 \cdot H_2O$	O1	O2	O3	O4	O5w		C.N.
Y	2/1	2/1	2/1	2/1	1/1		9
Na	2/1	2/1	2/1	2/1	0/0		8
S	1/1	1/1	1/1	1/1	0/0		4
H	0/0	0/0	0/0	0/0	1/2		1
C.N.	3	3	3	3	3		
$NaY[SO_4]_2$	O1	O2	O3	O4	O5	O6	C.N.
Y	1/1	2/2	2/1	2/1	1/1	0/0	8
Na	1/1	0/0	2/1	2/1	1/1	2/2	8
S1	0/0	0/0	2/1	0/0	1/1	1/1	4
S2	1/1	1/1	0/0	2/1	0/0	0/0	4
C.N.	3	3	3	3	3	3	

We became aware of a competing structure refinement for trigonal $NaY[SO_4]_2 \cdot H_2O$ (a = 681.91(3) pm, c = 1270.35(11) pm, c/a = 1.863) in space group $P3_121$ that was already in the progress of publication [54], simultaneous to our activities writing this article. The lower CSD deposition number (ours for $NaY[SO_4]_2 \cdot H_2O$ in space group $P3_221$: 2016596 versus the Chinese competitor one for $NaY[SO_4]_2 \cdot H_2O$ in space group $P3_121$: 2058909)

should grant us a priority, despite the almost identical results in both papers from the year 2021.

3.2. Thermal Analysis

A thermogravimetrical curve for the decomposition of $NaY[SO_4]_2 \cdot H_2O$ between 25 and 1400 °C is depicted in Figure 9.

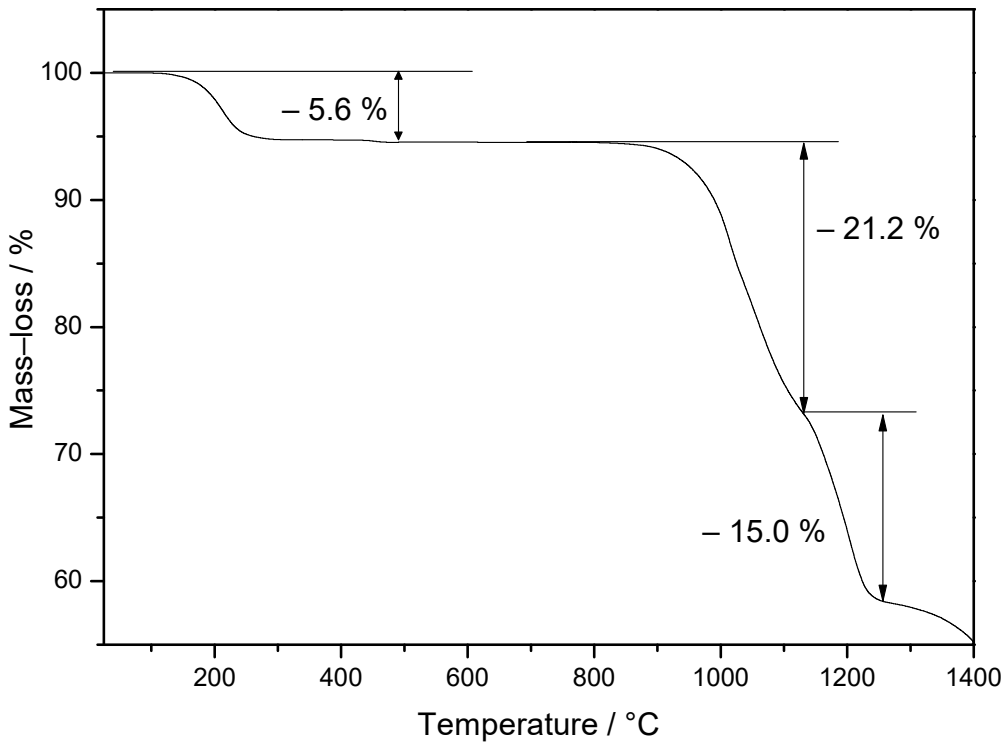

Figure 9. Thermogravimetrical curve of $NaY[SO_4]_2 \cdot H_2O$ between 25 and 1400 °C.

The first mass-loss at about 180 °C with 5.6% represents the release of water and the transformation from $NaY[SO_4]_2 \cdot H_2O$ (100% mass; M = 322.036 g/mol) to $NaY[SO_4]_2$ (94.4% mass; M = 304.021 g/mol). The second decomposition leads to a mixture of $Y_2O_2[SO_4]$ [55] with the crystal structure of monoclinic $La_2O_2[SO_4]$ [56] and $Eu_2O_2[SO_4]$ [57] or orthorhombic $Nd_2O_2[SO_4]$ [58] together with $Na_2[SO_4]$ [51,59], confirmed by powder X-ray diffraction experiments (Figures S1 and S2 in the Supplementary Information). For $Y_2O_2[SO_4]$, there are no known or other good crystal-structure data available, so there are differences in intensity and position, but the final decomposition step leads to a mixture of cubic Y_2O_3 with a bixbyite-type structure [60] and orthorhombic $Na_2[SO_4]$ [51,59] (Figure S3). The TG curve (Figure 9) appears to be similar to that of $NaRE[SO_4]_2 \cdot H_2O$ with RE = La, Ce, Nd, and Sm, which have been measured in 1994 by Kolcu and Zümreoğlu-Karan [18]. The dehydration temperature of the lanthanum compound is 297 °C and gets lower with decreasing RE^{3+}-cation radius along with the lanthanoid contraction [61]. With a dehydration temperature of 265 °C for the samarium compound, this trend is further confirmed with our yttrium analog at 180 °C.

Additional to the thermogravimetry, temperature-dependent X-ray diffraction experiments were performed (Figure 10).

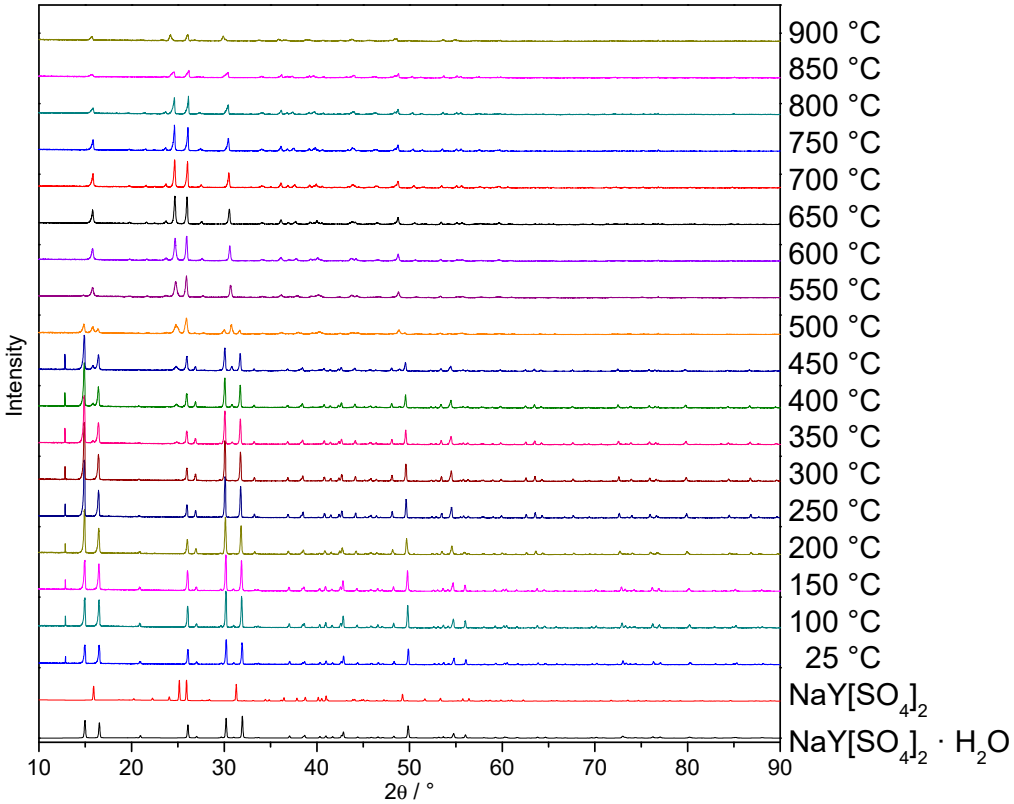

Figure 10. Temperature-dependent PXRD data of $NaY[SO_4]_2 \cdot H_2O$ in the range from 25 to 900 °C measured with Cu-Kα radiation (λ = 154.06 pm) in a reflection setting.

While the TG curve (Figure 9) shows a phase transformation from $NaY[SO_4]_2 \cdot H_2O$ to $NaY[SO_4]_2$ at 180 °C, the temperature-depending PXRD indicates the anhydrous compound for the first time at 350 °C. At 550 °C the water-containing compound could not be detected anymore. The XRD intensities became lower again with rising temperatures and suggest a starting decomposition of $NaY[SO_4]_2$ to $Y_2O_2[SO_4]$ and $Na_2[SO_4]$. The reflection at 12.8° resulted from the X-ray powder-diffractometer setting.

3.3. Luminescence-Spectroscopic Properties

Eu^{3+}-doped samples of $NaY[SO_4]_2 \cdot H_2O$ and $NaY[SO_4]_2$ under UV irradiation (λ = 254 nm) can be seen in Figure 11.

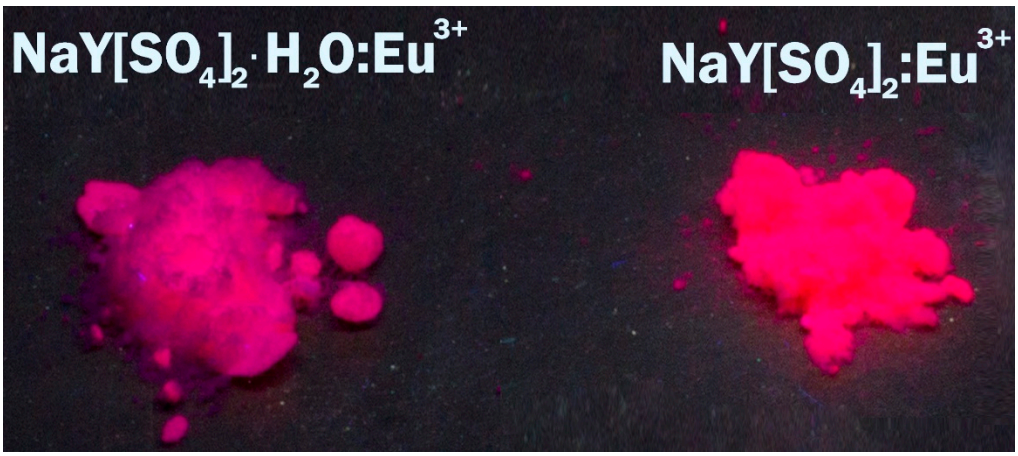

Figure 11. $NaY[SO_4]_2 \cdot H_2O:Eu^{3+}$ (**left**) and $NaY[SO_4]_2:Eu^{3+}$ (**right**) under UV irradiation (λ_{exc} = 254 nm).

Both compounds display a reflection spectrum, which is in line with plain white powders of good optical quality and high crystallinity, due to the lack of greying or defect bands. The absorption edge of the anhydrous compound at about 270 nm is assigned to the LMCT (ligand-to-metal charge-transfer) absorption band of Eu^{3+}, which is a typical energetic position of the LMCT process of Eu^{3+} in an oxidic environment [62]. The reflectance values at longer wavelengths were close to unity, pointing to a high optical quality of the prepared materials. In both reflection spectra (Figure 12), the typical Eu^{3+} absorption lines originating from the $^7F_0 \rightarrow {}^5L_6$ and $^7F_0 \rightarrow {}^5D_2$ transitions could be observed in the ranges of 395–397 nm and 450–470 nm, respectively [63].

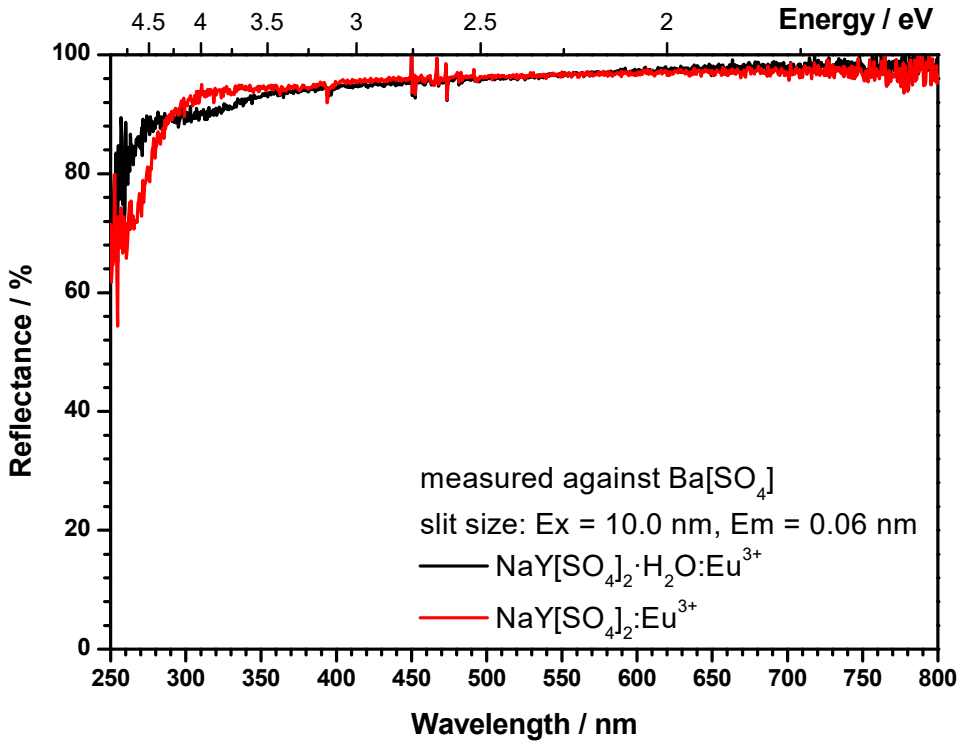

Figure 12. Reflection spectra of $NaY[SO_4]_2 \cdot H_2O:Eu^{3+}$ (black curve) and $NaY[SO_4]_2:Eu^{3+}$ (red curve).

Temperature-dependent excitation spectra of $NaY[SO_4]_2 \cdot H_2O:Eu^{3+}$ and $NaY[SO_4]_2:Eu^{3+}$ reveal the typical intraconfigurational 4f–4f transitions of Eu^{3+} between 280 and 550 nm [63,64] and the position of the LMCT of Eu^{3+} in the anhydrous compound. The LMCT band was located at 270 nm and was in good agreement with the position derived from the reflection spectrum. The excitation spectra of both compounds are plotted in Figure 13.

Noteworthy was the temperature-dependent excitation spectra of $NaY[SO_4]_2 \cdot H_2O:Eu^{3+}$, since a closer look at the UV-A range revealed a distinct change of the pattern of $^7F_0 \rightarrow {}^5L_6$ (390–405 nm) and $^7F_0 \rightarrow {}^5L_8 + {}^5G_J + {}^5L_9 + {}^5L_{10}$ (J = 2–6) (373–387 nm) transitions [65]. The thermal population of the $^7F_1$ level could explain some changes in the excitation line pattern. However, the shift and broadening of the most intense line of the $^7F_0 \rightarrow {}^5L_6$ multiplet at 394 nm from 400 K onwards pointed to a phase transition. This finding could be explained by the loss of water and the transformation of $NaY[SO_4]_2 \cdot H_2O:Eu^{3+}$ to $NaY[SO_4]_2:Eu^{3+}$ in good accordance with the results from thermal gravimetry (Figure 9). Temperature-dependent emission spectra of $NaY[SO_4]_2 \cdot H_2O:Eu^{3+}$ and $NaY[SO_4]_2:Eu^{3+}$ are shown in Figure 14.

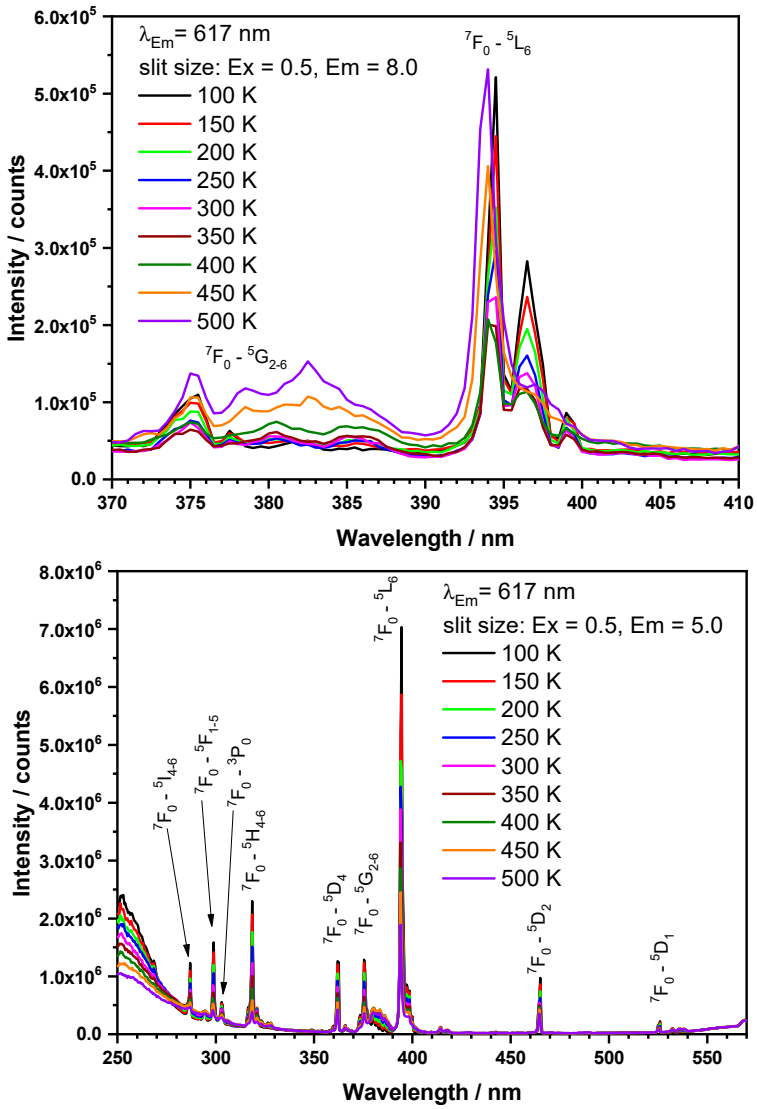

Figure 13. Excitation spectra of $NaY[SO_4]_2 \cdot H_2O:Eu^{3+}$ (**top**) and $NaY[SO_4]_2:Eu^{3+}$ (**bottom**) as a function of temperature between 100 and 500 K.

The emission spectra of Eu^{3+}-comprising materials consisted of the orange allowed magnetic-dipole (MD) transition $^5D_0 \rightarrow {}^7F_1$, the red parity-forbidden electric-dipole (ED) transition $^5D_0 \rightarrow {}^7F_2$, and further line multiplets in the deep red spectral range around 650 and 695 nm due to the ED transitions $^5D_0 \rightarrow {}^7F_3$ and $^5D_0 \rightarrow {}^7F_4$. For light sources and emissive displays, the emission spectrum should consist mainly of emission lines resulting from the $^5D_0 \rightarrow {}^7F_2$ transitions [66,67]. This means that the Eu^{3+} cation has to occupy a crystallographic site without inversion symmetry (see Figure 4 for symmetry examination). This also induces the deep red emission lines. Fortunately, the $^5D_0 \rightarrow {}^7F_2$ transition is hypersensitive and small deviations of the inversion symmetry strongly enhance the probability of the $^5D_0 \rightarrow {}^7F_2$ transitions. The intensity of the strongly forbidden transition $^5D_0 \rightarrow {}^7F_0$ is known to correlate with the linear terms of the crystal-field parameter and polarizability of the Eu^{3+} cation [67].

However, the emission spectrum of $NaY[SO_4]_2 \cdot H_2O:Eu^{3+}$ upon 395 nm excitation revealed the typical emission line pattern between 580 and 720 nm due to the $^5D_0 \rightarrow {}^7F_J$ (J = 0–4) transitions of Eu^{3+} [62,63,68]. Unfortunately, the signal-to-noise ratio is rather low, which points to a low quantum yield. Indeed, the determination of the quantum efficiency according to Kawamura [41] yielded a value of solely about 1%. Such a low quantum yield

can be explained by the presence of crystal water since the high phonon frequency of the O–H vibration of water quenches efficiently the Eu^{3+} luminescence [69].

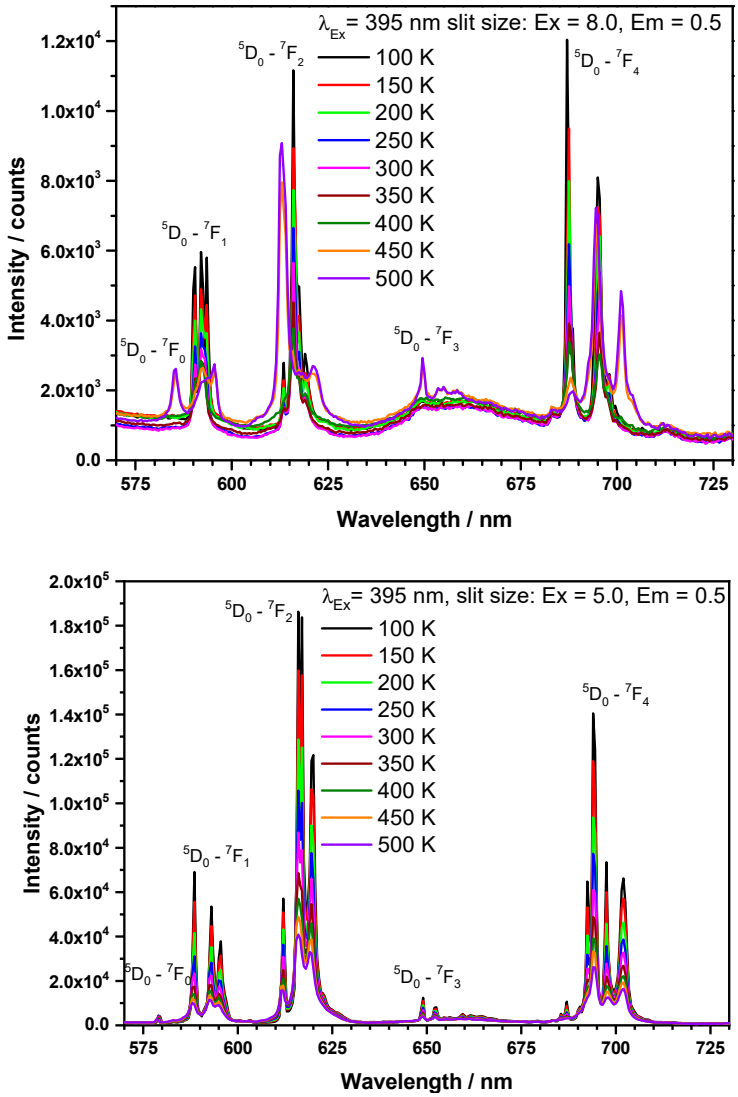

Figure 14. Temperature-dependent emission spectra of $NaY[SO_4]_2 \cdot H_2O:Eu^{3+}$ (**top**) and $NaY[SO_4]_2:Eu^{3+}$ (**bottom**) between 100 and 500 K upon 395 nm excitation.

As already observed for the excitation spectra, the temperature-dependent emission spectra of $NaY[SO_4]_2 \cdot H_2O:Eu^{3+}$ showed a distinct change once the temperature exceeded 400 K, resulting in the increase of intensity and the width of the $^5D_0 \rightarrow F_1$, $^5D_0 \rightarrow {}^7F_2$, and $^5D_0 \rightarrow {}^7F_4$ transitions, as well as the appearance of the $^5D_0 \rightarrow {}^7F_0$ transition, which was absent at room temperature. This change again points to a phase transition, i.e., the transformation of $NaY[SO_4]_2 \cdot H_2O:Eu^{3+}$ to $NaY[SO_4]_2:Eu^{3+}$, which goes along with an increase of the crystal-field strength causing a larger energetic spread of the Stark components of the above mentioned $^5D_0 \rightarrow {}^7F_J$, transitions. This finding was in good agreement with the decline of the coordination number from 9 to 8 and a shorter average Y–O distance. However, even though the emission spectra of the anhydrous sample obtained after the phase transition resembled that of the as-prepared anhydrous sample, the emission spectra were not completely the same. We assumed that after the phase transition a higher defect density remained, which resulted in line-broadening and a lower signal-to-noise ratio since, without further high-temperature treatment, defects caused by the water removal cannot be healed. In contrast, the as-prepared samples of anhydrous

$NaY[SO_4]_2:Eu^{3+}$ showed a much higher quantum yield. This value was determined to be almost around 20%, which also explained the much better signal-to-noise ratio of the respective emission spectra as a function of temperature (Figure 14, bottom).

The CIE1931 color coordinates of $NaY[SO_4]_2:Eu^{3+}$ are at $x = 0.65$ and $y = 0.35$, while the temperature impact is rather low, branding the substance as a stable color-consistent material for application in displays or fluorescent light sources [1]. However, the magnification of the color space in Figure 15 demonstrates that the color point shifts slightly to the orange range, which can be caused by the reduction of the asymmetry ratio $^5D_0 \rightarrow {}^7F_2$ $/^5D_0 \rightarrow {}^7F_1$ [63] or by the reduction of the covalency related to the $^5D_0 \rightarrow {}^7F_4/^5D_0 \rightarrow {}^7F_J$ ratio [3]. However, both effects are in line with a thermal expansion of the crystals and the Eu^{3+} site causes a decrease of the covalent interaction between Eu^{3+} and oxygen and an increase of the local symmetry.

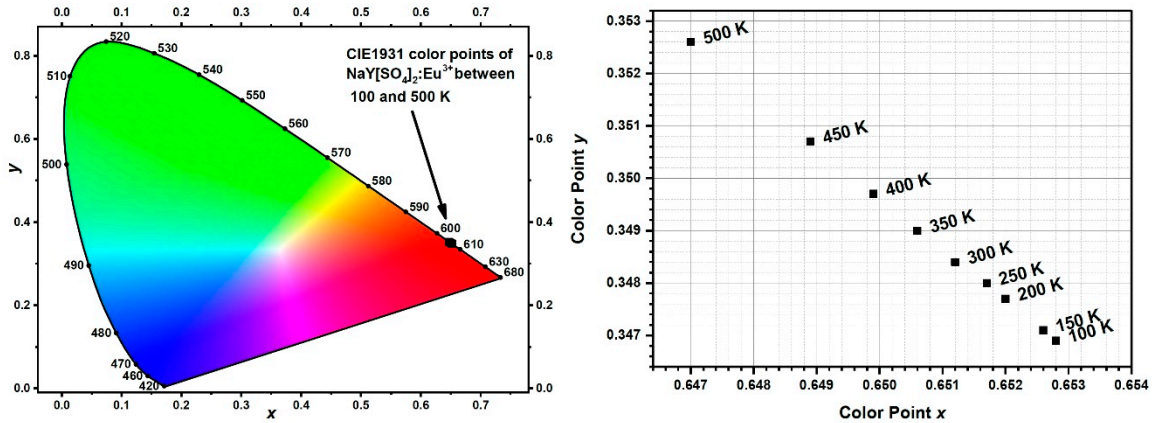

Figure 15. Temperature-dependent CIE1931 color points of the anhydrous $NaY[SO_4]_2:Eu^{3+}$ between 100 and 500 K upon 395 nm excitation (**left**) and zoom for the magnification of the red area of the color triangle (**right**).

Noteworthy were the intensities of the temperature-dependent emission spectra of $NaY[SO_4]_2 \cdot H_2O:Eu^{3+}$ as depicted in Figure 16. While the intensity decreased between 100 and 300 K due to typical thermal quenching, it increased again between 300 and 500 K. This effect was caused by the phase transition towards the formation of the more efficiently luminescent $NaY[SO_4]_2:Eu^{3+}$ upon increasing the temperature.

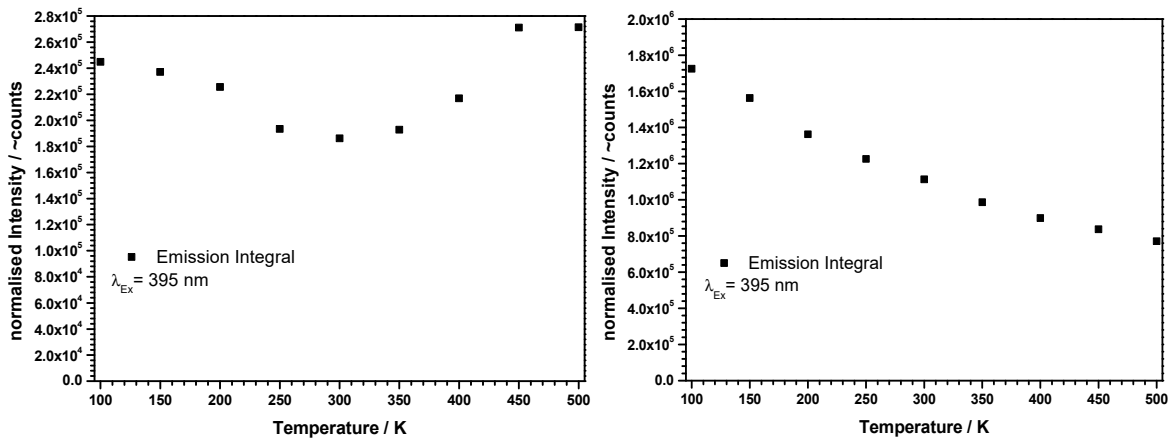

Figure 16. Temperature-dependent emission integrals of $NaY[SO_4]_2 \cdot H_2O:Eu^{3+}$ (**left**) and $NaY[SO_4]_2:Eu^{3+}$ (**right**) between 100 and 500 K upon 395 nm excitation.

In contrast, the temperature-dependent emission spectra of $NaY[SO_4]_2:Eu^{3+}$ itself show a typical decrease of the intensity or quantum yield of Eu^{3+} phosphors with increasing temperature [63].

Finally, we investigated the time-dependent luminescence (Figure 17) of the $^5D_0 \rightarrow {}^7F_2$ transition of Eu^{3+} at 617 nm upon 395 nm excitation of $NaY[SO_4]_2 \cdot H_2O:Eu^{3+}$ and $NaY[SO_4]_2:Eu^{3+}$. As discussed before, $NaY[SO_4]_2 \cdot H_2O:Eu^{3+}$ shows a peculiar behavior due to the phase transition between 400 and 500 K, which means that the decay time increases from 550 µs at 100 K to about 930 µs at 500 K. At the same time, the decay curves become bi-exponential, which points to the formation of a novel phase with a prolonged decay time and enhanced internal quantum efficiency. The decay curves of $NaY[SO_4]_2:Eu^{3+}$ between 100 and 500 K were almost perfectly mono-exponential over three orders of magnitude, while the derived decay times remained rather constant, as proven by the just slight decline from 2.35 ms to 2.20 ms. This finding meant that the internal quantum yield stayed quite stable, and thus, thermal quenching of the Eu^{3+} photoluminescence is a minor issue.

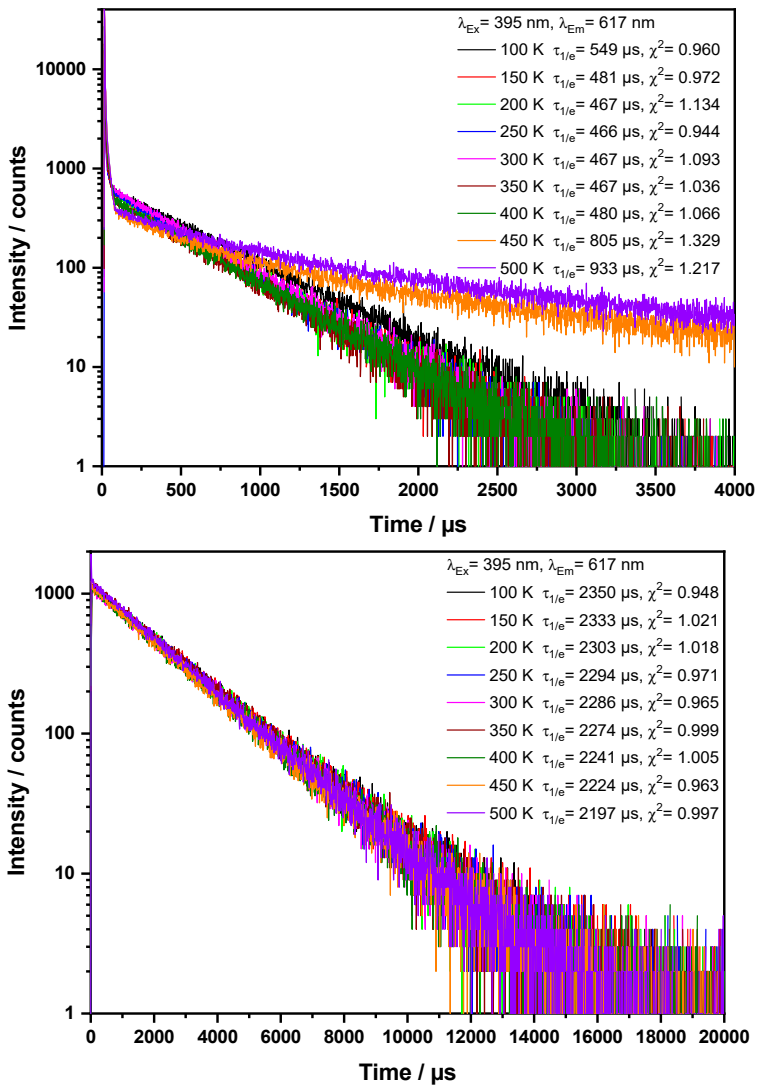

Figure 17. Temperature-dependent decay curves of $NaY[SO_4]_2 \cdot H_2O:Eu^{3+}$ (**top**) and $NaY[SO_4]_2:Eu^{3+}$ (**bottom**) between 100 and 500 K upon 395 nm excitation.

3.4. IR and Raman Studies of $NaY[SO_4]_2 \cdot H_2O$ and $NaY[SO_4]_2$

The Raman and IR spectra of $NaY[SO_4]_2 \cdot H_2O$ and $NaY[SO_4]_2$ are shown together with those of $Y_2[SO_4]_3 \cdot 8\ H_2O$ and $Na_2[SO_4]$ in Figure 18 and the values are given in Table 6 compared to the literature data for $Y_2[SO_4]_3$ [69] and $Na_2[SO_4]$ (thenardite) [70]. The vibration at about 2300 cm^{-1} represents CO_2 in the laboratory environment. While the ideal $[SO_4]^{2-}$ anion with T_d symmetry should only have four visible vibration bands (ν_{as}

and δ_{as}: IR and Raman active, ν_s and δ_s: only Raman active), in the measured solid-state samples there were more bands measured. This was because of the no longer ideal $[SO_4]^{2-}$ units and their considerable symmetry reduction.

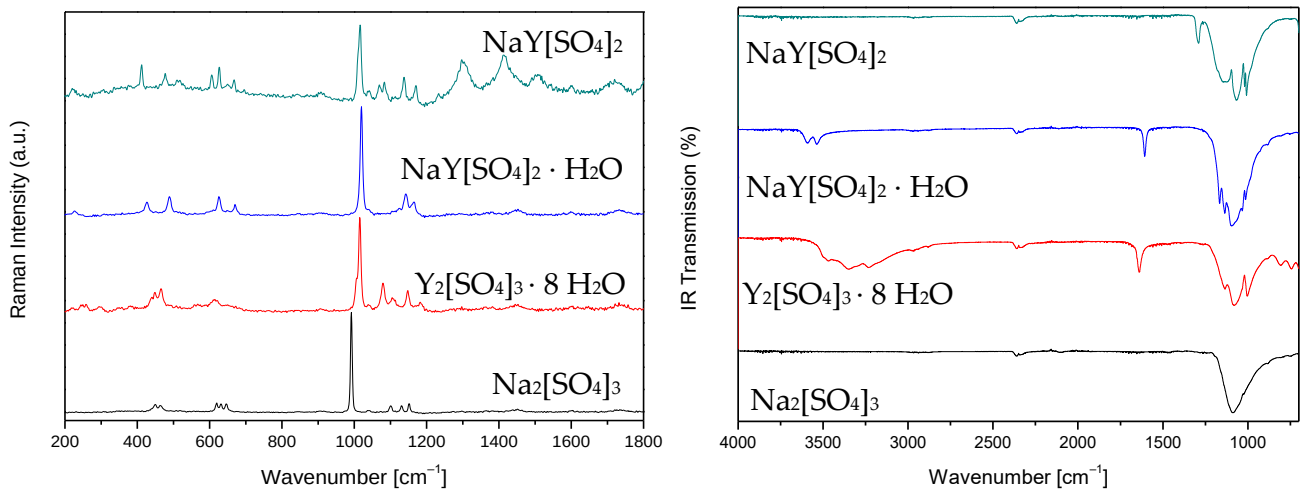

Figure 18. Raman (**left**) and IR spectra (**right**) of $NaY[SO_4]_2$, $NaY[SO_4]_2 \cdot H_2O$, $Y_2[SO_4]_3 \cdot 8\ H_2O$, and $Na_2[SO_4]$ (from top to bottom).

Table 6. Raman (**black**) and IR vibration values (**blue**) of $NaY[SO_4]_2$ and $NaY[SO_4]_2 \cdot H_2O$ as compared to those of $Y_2[SO_4]_3 \cdot 8\ H_2O$, $Y_2[SO_4]_3$ [69], and $Na_2[SO_4]$ (thenardite) [70].

$\tilde{\nu}$ [cm^{-1}]	$NaY[SO_4]_2$	$NaY[SO_4]_2 \cdot H_2O$	$Y_2[SO_4]_3 \cdot 8\ H_2O$	$Y_2[SO_4]_3$ *	$Na_2[SO_4]$ (thenardite) *
$[SO_4]^{2-}$ δ_s 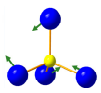	413, 479	429, 492	442, 450, 467	452, 484, 504	451, 466
δ_{as} 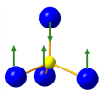	608, 629, 669 667, 685	628, 669 600, 626, 660	618 638, 652, 688, 743	609, 654	621, 632, 647 609, 634, 668
ν_s 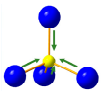	1015, 1046 1007, 1010, 1068	1020 1012, 1032, 1092	1015 1002, 1080, 1032	1013	933
ν_{as} 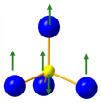	1080, 1085, 1140, 1172 1120, 1140, 1289	1145, 1168 1135, 1165	1080, 1088, 1112, 1146 1132	1122, 1145, 1184	1102, 1129, 1152 1090
H_2O $\nu_{as,s}$ 		3536, 3592	3229, 3348, 3467		
δ 		1606	1640		

* Raman data of $Y_2[SO_4]_3$ and $Na_2[SO_4]$ from literature [69,70], IR data measured in this work.

4. Conclusions

Phase-pure white powder and even colorless single crystals of sodium yttrium oxosulfate monohydrate $NaY[SO_4]_2 \cdot H_2O$ could be synthesized hydrothermally from a mixture of $Na_2[SO_4]$ and $Y_2[SO_4]_3 \cdot 8\ H_2O$ in demineralized water. The anhydrate $NaY[SO_4]_2$ was obtained by thermal decomposition at temperatures above 180 °C and is stable up to 800 °C. While the trigonal crystal structure of $NaY[SO_4]_2 \cdot H_2O$ was solved from single-crystal X-ray diffraction data in space group $P3_221$, the monoclinic crystal structure of $NaY[SO_4]_2$ was refined with *Rietveld* methods from powder X-ray diffraction data in space group $P2_1/m$. The Na^+ cations are coordinated by eight oxygen atoms from six tetrahedral $[SO_4]^{2-}$ anions in both compounds and the coordination numbers of the Y^{3+} cations in the hydrate amount to nine (eight oxygen atoms from six $[SO_4]^{2-}$ units plus one from a water molecule) and eight again in the anhydrate (eight oxygen atoms from six $[SO_4]^{2-}$ anions). Both compounds suit as red-emitting luminescent materials, if doped with 0.5 % Eu^{3+}, as shown by luminescence spectroscopy, but the anhydrate $NaY[SO_4]_2$:Eu^{3+} exhibits an almost twenty times higher quantum efficiency than the monohydrate $NaY[SO_4]_2 \cdot H_2O$:Eu^{3+} owing to the water of hydration, which works as a vibrational quencher. The almost perfect monoexponential decay curves of the anhydrate $NaY[SO_4]_2$:Eu^{3+} and thus the lack of afterglow also prove the presence of a material with high quality, i.e., a low defect density.

Supplementary Materials: The Supplementary Material contains PXRD data from a sample after thermal treatment from 1000 °C (Figure S1 and S2) and 1400 °C (Figure S3) after the thermogravimetry experiment. They are available online at https://www.mdpi.com/article/10.3390/cryst11060575/s1.

Author Contributions: C.B. synthesized the pure and the Eu^{3+}-doped compounds, which are described here, and measured their IR and Raman spectra. C.B. and T.S. solved the crystal structures of both compounds. T.S. contributed the reagents, the materials, the scientific equipment, and the infrastructure for synthesis, IR, and Raman spectroscopy. D.E. and T.J. measured and interpreted the Eu^{3+} luminescence of both doped compounds. The paper was written by all authors. All authors have read and agreed to the published version of the manuscript.

Funding: This research was funded by the State of Baden-Württemberg (Stuttgart).

Data Availability Statement: Crystallographic data are available in the ICSD-Database with the CSD-numbers 2016596 for $NaY[SO_4]_2 \cdot H_2O$ and 2072719 for $NaY[SO_4]_2$.

Acknowledgments: We thank Falk Lissner for the single-crystal X-ray diffraction measurements, Patrik Djendjur for the thermal analyses, and Jean-Louis Hoslauer for the temperature-dependent PXRD experiments.

Conflicts of Interest: The authors declare no conflict of interest.

References

1. Jüstel, T.; Nikol, H.; Ronda, C. New Developments in the Field of Luminescent Materials for Lighting and Displays. *Angew. Chem. Int. Ed.* **1998**, *37*, 3084–3103. [CrossRef]
2. Feldmann, C.; Jüstel, T.; Ronda, C.R.; Schmidt, P.J. Inorganic Luminescent Materials: 100 Years of Research and Application. *Adv. Funct. Mater.* **2003**, *13*, 511–516. [CrossRef]
3. Skaudzius, R.; Katelnikovas, A.; Enseling, D.; Kareiva, A.; Jüstel, T. Dependence of the $^5D_0 \rightarrow {}^7F_4$ transitions of Eu^{3+} on the local environment in phosphates and garnets. *J. Lumin.* **2014**, *147*, 290–294. [CrossRef]
4. Laufer, S.; Strobel, S.; Schleid, T.; Cybinska, J.; Mudring, A.-V.; Hartenbach, I. Yttrium(III) Oxomolybdates(VI) as Potential Host Materials for Luminescence Applications: An Investigation of Eu^{3+}-Doped $Y_2[MoO_4]_3$ and $Y_2[MoO_4]_2[Mo_2O_7]$. *New J. Chem.* **2013**, *37*, 1919–1926. [CrossRef]
5. Goerigk, F.C.; Paterlini, V.; Dorn, K.V.; Mudring, A.-V.; Schleid, T. Synthesis and Crystal Structure of the Short $LnSb_2O_4Br$ Series (*Ln* = Eu–Tb) and Luminescence Properties of Eu^{3+}-Doped Samples. *Crystals* **2020**, *10*, 1089. [CrossRef]
6. Popovic, E.J.; Imre-Lucaci, F.; Muresan, L.; Stefan, M.; Bica, E.; Grecu, R.; Indrea, E. Spectral investigations on niobium and rare earth activated yttrium tantalate powders. *J. Optoelectron. Adv. Mater.* **2008**, *10*, 2334–2337.
7. Ledderboge, F.; Nowak, J.; Massonne, H.-J.; Förg, K.; Höppe, H.A.; Schleid, T. High-Pressure Investigations of Yttrium(III) Oxoarsenate(V): Crystal Structure and Luminescence Properties of Eu^{3+}-Doped Scheelite-Type $Y[AsO_4]$ from Xenotime-Type Precursors. *J. Solid State Chem.* **2018**, *263*, 65–71. [CrossRef]

8. Cybińska, J. Temperature dependent morphology variation of red emitting microcrystalline $YPO_4:Eu^{3+}$ fabricated by hydrothermal method. *Opt. Mater.* **2017**, *65*, 88–94. [CrossRef]
9. Chang, H.-Y.; Chen, F.-S.; Lu, C.-H. Preparation and luminescence characterization of new carbonate ($Y_2(CO_3)_3 \cdot n\ H_2O:Eu^{3+}$) phosphors via the hydrothermal route. *J. Alloys Compd.* **2011**, *509*, 10014–10019. [CrossRef]
10. Lindgren, O. The Crystal Structure of Sodium Cerium(III) Sulfate Hydrate, $NaCe(SO_4)_2 \cdot H_2O$. *Acta Chem. Scand.* **1977**, *31*, 591–594. [CrossRef]
11. Wu, C.-D.; Liu, Z.-Y. Hydrothermal synthesis of a luminescent europium(III) sulfate with three-dimensional chiral framework structure. *J. Solid State Chem.* **2006**, *179*, 3500–3504. [CrossRef]
12. Zhai, B.; Li, Z.; Zhang, C.; Zhang, F.; Zhang, X.; Zhang, F.; Cao, G.; Li, S.; Yang, X. Three rare Ln–Na heterometallic 3D polymers based on sulfate anion: Syntheses, structures, and luminescence properties. *Inorg. Chem. Commun.* **2016**, *63*, 16–19. [CrossRef]
13. Perles, J.; Fortes-Revilla, C.; Gutiérrez-Puebla, E.; Iglesias, M.; Monge, M.Á.; Ruiz-Valero, C.; Snejko, N. Synthesis, Structure, and Catalytic Properties of Rare-Earth Ternary Sulfates. *Chem. Mater.* **2005**, *17*, 2701–2706. [CrossRef]
14. Paul, A.K.; Kanagaraj, R. Synthesis, Characterization, and Crystal Structure Analysis of New Mixed Metal Sulfate $NaPr(SO_4)_2(H_2O)$. *J. Struct. Chem.* **2019**, *60*, 477–484. [CrossRef]
15. Blackburn, A.C.; Gerkin, R.E. Sodium lanthanum(III) sulfate monohydrate, $NaLa(SO_4)_2 \cdot H_2O$. *Acta Crystallogr.* **1994**, *50*, 835–838. [CrossRef]
16. Blackburn, A.C.; Gerkin, R.E. Redetermination of sodium cerium(III) sulfate monohydrate, $NaCe(SO_4)_2 \cdot H_2O$. *Acta Crystallogr.* **1995**, *51*, 2215–2218. [CrossRef] [PubMed]
17. Kolcu, Ö.; Zümreoğlu-Karan, B. Nonisothermal Dehydration Kinetics of Sodium-Light Lanthanoid Double Sulfate Monohydrates. *Thermochim. Acta* **1997**, *296*, 135–139. [CrossRef]
18. Kolcu, Ö.; Zümreoğlu-Karan, B. Thermal Properties of Sodium-Light-Lanthanoid Double Sulfate Monohydrates. *Thermochim. Acta* **1994**, *240*, 185–198. [CrossRef]
19. Iyer, P.N.; Natarajan, P.R. Double Sulphates of Plutonium(III) and lanthanides with sodium. *J. Less Common Met.* **1989**, *146*, 161–166. [CrossRef]
20. Kazmierczak, K.; Höppe, H.A. Syntheses, crystal structures and vibrational spectra of $KLn(SO_4)_2 \cdot H_2O$ (*Ln* = La, Nd, Sm, Eu, Gd, Dy). *J. Solid State Chem.* **2010**, *183*, 2087–2094. [CrossRef]
21. Jemmali, M.; Walha, S.; Ben Hassen, R.; Vaclac, P. Potassium cerium(III) bis(sulfate) monohydrate, $KCe(SO_4)_2 \cdot H_2O$. *Acta Crystallogr.* **2005**, *61*, i73–i75. [CrossRef]
22. Iskhakova, L.D.; Sarukhanyan, N.L.; Shchegoleva, T.M.; Trunov, V.K. The crystal structure of $KPr(SO_4)_2 \cdot H_2O$. *Kristallografiya* **1985**, *30*, 474–479.
23. Lyutin, V.I.; Safyanov, Y.N.; Kuzmin, E.A.; Ilyukhin, V.V.; Belov, N.V. Rhomb evaluation of the crystal structure of K-Tb double sulfate. *Kristallografiya* **1974**, *19*, 376–378.
24. Robinson, P.D.; Jasty, S. Rubidium Cerium Sulfate Monohydrate, $RbCe(SO_4)_2 \cdot H_2O$. *Acta Crystallogr.* **1998**, *C54*, IUC9800021. [CrossRef]
25. Prokofev, M.V. Crystal structure of the double sulfate of rubidium and holmium. *Kristallografiya* **1981**, *26*, 598–600.
26. Sarukhanyan, N.L.; Iskhakova, L.D.; Trunov, V.K.; Ilyukhin, V.V. Crystal structure of $RbLn(SO_4)_2(H_2O)$ (Ln = Gd, Ho, Yb). *Koord. Khim.* **1984**, *10*, 981–987.
27. Audebrand, N.; Auffrédic, J.-P.; Louër, D. Crystal structure of silver cerium sulfate hydrate, $AgCe(SO_4)_2 \cdot H_2O$. *Z. Kristallogr.* **1998**, *213*, 481. [CrossRef]
28. Cheng, S.; Wu, Y.; Mei, D.; Wen, S.; Doert, T.H. Synthesis, Crystal Structures, Spectroscopic Characterization, and Thermal Analyses of the New Bismuth Sulfates $NaBi(SO_4)_2 \cdot H_2O$ and $ABi(SO_4)_2$ (*A* = K, Rb, Cs). *Z. Anorg. Allg. Chem.* **2020**, *646*, 1688–1695. [CrossRef]
29. Song, Y.; Zou, H.; Sheng, Y.; Zheng, K.; You, H. 3D Hierarchical Architectures of Sodium Lanthanide Sulfates: Hydrothermal Synthesis, Formation Mechanisms, and Luminescence Properties. *J. Phys. Chem. C* **2011**, *115*, 19463–19469. [CrossRef]
30. Kampf, A.R.; Nash, B.P.; Marty, J. Chinleite-(Y), $NaY(SO_4)_2 \cdot H_2O$, a new rare-earth sulfate mineral structurally related to bassanite. *Mineral. Mag.* **2017**, *81*, 909–916. [CrossRef]
31. Sirotinkine, S.P.; Tchijov, S.M.; Pokrovskii, A.N.; Kovba, L.M. Structure cristalline de sulfates doubles de sodium et de terres rares. *J. Less Common Met.* **1978**, *58*, 101–105. [CrossRef]
32. Chizhov, S.M.; Pokrovskii, A.N.; Kovba, L.M. The crystal structure of alpha-$NaTm(SO_4)_2$. *Kristallografiya* **1982**, *27*, 997–998.
33. Chizhov, S.M.; Pokrovskii, A.N.; Kovba, L.M. The crystal structure of $NaLa(SO_4)_2$. *Kristallografiya* **1981**, *26*, 834–836.
34. Wickleder, M.S.; Büchner, O. The Gold Sulfates $MAu(SO_4)_2$ (*M* = Na, K, Rb). *Z. Naturforsch.* **2001**, *56*, 1340–1343. [CrossRef]
35. Denisenko, Y.G.; Atuchin, V.V.; Molokeev, M.S.; Aleksandrovsky, A.S.; Krylov, A.S.; Oreshonkov, A.S.; Volkova, S.S.; Andreev, O.V. Structure, Thermal Stability, and Spectroscopic Properties of Triclinic Double Sulfate $AgEu(SO_4)_2$ with Isolated SO_4 Groups. *Inorg. Chem.* **2018**, *57*, 13279–13288. [CrossRef]
36. Sheldrick, G.M. A short history of SHELX. *Acta Crystallogr.* **2008**, *64*, 112–122. [CrossRef] [PubMed]
37. Sheldrick, G.M. *Program. Suite for the Solution and Refinement of Crystal Structures*; Univeristy of Göttingen: Göttingen, Germany, 1997.
38. Bärnighausen, W.; Herrendorf, H. *Habitus*; Program for the Optimization of the Crystal Shape for Numerical Absorption Correction in X-SHAPE; Karlsruhe: Gießen, Germany, 1993.

39. Rodríguez-Carvajal, J. Recent advances in magnetic structure determination by neutron powder diffraction. *Phys. B Condens. Matter* **1993**, *192*, 55–69. [CrossRef]
40. Roisnel, T.; Rodríguez-Carvajal, J. WinPLOTR: A Windows tool for powder diffraction analysis. In *Materials Science Forum. Proceedings of the European Powder Diffraction Conference*; CiteSeerX: State College, PA, USA, 2001.
41. Kawamura, Y.; Sasabe, H.; Adachi, C. Simple Accurate System for Measuring Absolute Photoluminescence Quantum Efficiency in Organic Solid-State Thin Films. *Jpn. J. Appl. Phys.* **2004**, *43*, 7729–7730. [CrossRef]
42. Downloaded at 10 April 2021. Available online: https://www.osram.us/cb/tools-and-resources/applications/led-colorcalculator/index.jsp (accessed on 27 April 2021).
43. Smet, P.F.; Parmentier, A.B.; Poelman, D. Selecting Conversion Phosphors for White Light-Emitting Diodes. *J. Electrochem. Soc.* **2011**, *158*, 37. [CrossRef]
44. Fischer, R.X.; Tillmanns, E. The equivalent isotropic displacement factor. *Acta Crystallogr.* **1988**, *44*, 775–776. [CrossRef]
45. Held, P.; Wickleder, M.S. Yttrium(III) sulfate octahydrate. *Acta Crystallogr.* **2003**, *59*, i98–i100. [CrossRef]
46. Wickleder, M.S. Wasserfreie Sulfate der Selten-Erd-Elemente: Synthese und Kristallstruktur von $Y_2(SO_4)_3$ und $Sc_2(SO_4)_3$. *Z. Anorg. Allg. Chem.* **2000**, *626*, 1468–1472. [CrossRef]
47. Degtyarev, P.A.; Pokrovskii, A.N.; Kovba, L.M. Crystal structure of the anhydrous double sulfate $KPr(SO_4)_2$. *Kristallografiya* **1978**, *23*, 840–843.
48. Degtyarev, P.A.; Korytnaya, F.M.; Pokrovskii, A.N.; Kovba, L.M. Crystal structure of the anhydrous double sulfate of potassium and neodymium $KNd(SO_4)_2$. *Vestn. Mosk. Univ. Seriya 2 Khimiya* **1997**, *16*, 705–708.
49. Iskhakova, L.D.; Gasanov, Y.M.; Trunov, V.K. Crystal structure of the monoclinic modification of $KNd(SO_4)_2$. *J. Struct. Chem.* **1988**, *29*, 242–246. [CrossRef]
50. Sarukhanyan, N.L.; Iskhakova, L.D.; Trunov, V.K. The crystal structure of $KEr(SO_4)_2$. *Kristallografiya* **1985**, *30*, 274–278.
51. Zachariasen, W.H.; Ziegler, G.E. The crystal structure of anhydrous sodium sulfate Na_2SO_4. *Z. Kristallogr.* **1932**, *81*, 92–101. [CrossRef]
52. Ruben, H.W.; Templeton, D.H.; Rosenstein, R.D.; Olovsson, I. Crystal Structure and Entropy of Sodium Sulfate Decahydrate. *J. Am. Chem. Soc.* **1961**, *83*, 820–824. [CrossRef]
53. Brese, N.E.; O'Keeffe, M. Bond-valence parameters for solids. *Acta Crystallogr.* **1991**, *47*, 192. [CrossRef]
54. Wu, C.; Lin, L.; Wu, T.; Huang, Z.; Zhang, C. Deep-ultraviolet transparent alkali metal-rare earth metal sulfate $NaY(SO_4)_2 \cdot H_2O$ as a nonlinear optical crystal: Synthesis and characterization. *CrystEngComm* **2021**, *23*, 2945–2951. [CrossRef]
55. Kijima, T.; Shinbori, T.; Sekita, M.; Uota, M.; Sakai, G. Abnormally enhanced Eu^{3+} emission in $Y_2O_2SO_4$:Eu^{3+} inherited from their precursory dodecylsulfate-templated concentric-layered nanostructure. *J. Lumin.* **2008**, *128*, 311–316. [CrossRef]
56. Zhukov, S.; Yatsenko, A.; Chernyshev, V.; Trunov, V.; Tserkovnaya, E.; Antson, O.; Hölsä, J.; Baulés, P.; Schenk, H. Structural study of lanthanum oxysulfate $(LaO)_2SO_4$. *Mater. Res. Bull.* **1997**, *32*, 43–50. [CrossRef]
57. Hartenbach, I.; Schleid, T. Serendipitous Formation of Single-Crystalline $Eu_2O_2[SO_4]$. *Z. Anorg. Allg. Chem.* **2002**, *628*, 2171. [CrossRef]
58. Golovnev, N.N.; Molokeev, M.S.; Vereshchagin, S.N.; Atuchin, V.V. Synthesis and thermal transformation of a neodymium(III) complex $[Nd(HTBA)_2(C_2H_3O_2)(H_2O)_2]\cdot 2\ H_2O$ to non-centrosymmetric oxosulfate $Nd_2O_2SO_4$. *J. Coord. Chem.* **2015**, *68*, 1865–1877. [CrossRef]
59. Niggli, A. Die Raumgruppe von Na_2CrO_4. *Acta Crystallogr.* **1954**, *7*, 776. [CrossRef]
60. Brauer, G.; Gradinger, H. Über heterotype Mischphasen bei Seltenerdoxyden. *Z. Anorg. Allg. Chem.* **1954**, *276*, 209–226. [CrossRef]
61. Shannon, R.D. Revised effective ionic radii and systematic studies of interatomic distances in halides and chalcogenides. *Acta Crystallogr.* **1976**, *32*, 751. [CrossRef]
62. Blasse, B.; Grabmaier, C. *Luminescent Materials*; Springer: Berlin/Heidelberg, Germany; New York, NY, USA, 1994; ISBN 3-540-58019-0.
63. Binnemans, K. Interpretation of europium(III) spectra. *Coord. Chem. Rev.* **2015**, *295*, 1–45. [CrossRef]
64. Dorenbos, P. The Eu^{3+} charge transfer energy and the relation with the band gap of compounds. *J. Lumin.* **2005**, *111*, 89–104. [CrossRef]
65. Baur, F.; Jüstel, T. New Red-Emitting Phosphor $La_2Zr_3(MoO_4)_9$:Eu^{3+} and the Influence of Host Absorption on its Luminescence Efficiency. *Aust. J. Chem.* **2015**, *68*, 1727–1734. [CrossRef]
66. Baur, F.; Jüstel, T. Eu^{3+} activated molybdates—Structure property relations. *Opt. Mater. X* **2019**, *1*, 100015. [CrossRef]
67. Blasse, G. Reminiscencies of a quenched luminescence investigatory. *J. Lumin.* **2002**, *100*, 65–67. [CrossRef]
68. Frech, R.; Cole, R.; Dharmasena, G. Raman Spectroscopic Studies of $Y_2(SO_4)_3$ Substitution in $LiNaSO_4$ and $LiKSO_4$. *J. Solid State Chem.* **1993**, *105*, 151–160. [CrossRef]
69. Supkowski, R.M.; Horrocks, W.D.W. On the determination of the number of water molecules, q, coordinated to europium(III) ions in solution from luminescence decay lifetimes. *Inorg. Chim. Acta* **2002**, *340*, 44–48. [CrossRef]
70. Prieto-Taboada, N.; Fdez-Ortiz de Vallejuelo, S.; Veneranda, M.; Lama, E.; Castro, K.; Arana, G.; Larrañaga, A.; Madariaga, J.M. The Raman spectra of the Na_2SO_4–K_2SO_4 system: Applicability to soluble salts studies in built heritage. *J. Raman Spectrosc.* **2019**, *50*, 175–183. [CrossRef]